IEEE Transactions on Robotics (T-RO) paper, presented at ICRA 2026, Vienna, Austria. Cite as T-RO paper.

A MagsL-HUD Endoscopic System for Magnetic Compression Anastomosis Surgery in Unstructured Endoluminal Environment

Yichong Sun, *Student Member, IEEE*, Yitian Xian, *Member, IEEE*, Ruoyu Xu, Wai Shing Chan, *Graduate Student Member, IEEE*, Hon Chi Yip, Philip Wai Yan Chiu, and Zheng Li, *Senior Member, IEEE*

***Abstract*—Magnetic compression anastomosis (MCA) offers a promising solution for minimally invasive anastomosis surgery. However, current MCA schemes lack safe, real-time localization, and guidance for compression magnets, hindering surgeons' ability to control the compression magnets effectively in complex, unstructured endoluminal environments. To address these limitations, this article introduces the MagsL-HUD endoscopic system, a novel solution that enables multimagnetic six-degree-of-freedom (six-DoF) localization and head-up display (HUD) guidance within the endoscopic view (EV). Specifically, the system integrates a developed Endo-MagCap device with an orthogonal magnet configuration, along with a magnetic sensor array, to achieve real-time full-pose localization. An endoscopic camera model is incorporated for HUD visualization, enhancing intuitive interaction for surgeons' better-informed decisions. Eventually, the effectiveness of the MagsL-HUD endoscopic system is validated through laboratory experiments and ex vivo animal trials. The system demonstrates six-DoF tracking accuracy with average errors of 0.0070 m and 0.1437 rad, and 0.0071 m and 0.1721 rad in the designed trajectory cases for two compression magnets, respectively. Additionally, ex vivo porcine tests confirm the system's feasibility and applicability, successfully performing a stomach-colon MCA surgery with a final compression gap of approximately 0.00247 m. Further comparative studies demonstrate that the MagsL-HUD method has a compression success rate of 71.4% versus 42.9% of the non-HUD approaches in the designed tests. This work represents a significant step toward the clinical adoption of magnetic-assisted endoscopy for minimally invasive anastomosis surgeries, holding substantial practical significance for improving the safety and efficacy of MCA procedures in complex, unstructured endoluminal environments.**

***Index Terms*—Head-up display endoscopy, magnetic-assisted surgery, medical robotics, multimagnetic localization, ex vivo trial.**

KEY SYMBOL NOMENCLATURE

$\mathbb{N}^+$	Natural numbers without 0.
$\mathbb{N}$	Natural numbers.
$\mathbb{R}^+$	Positive reals.
$\mathbb{R}^{j\times k}$	Real matrices in size $j \times k$.
$\mathbb{O}_{j\times k}$ or $\mathbb{I}_{j\times k}$	Zero or identity matrices in size $j \times k$.
$\mathbb{SO}(3)$	Special orthogonal group in $\mathbb{R}^{3\times 3}$.
$\mathbb{SE}(3)$	Special Euclidean group in $\mathbb{SO}(3) \times \mathbb{R}^3$.
$\mathbb{H}$	Four-space of quaternion.
$\otimes$	Product of two quaternion.
$X^\top$	Transpose of matrix X.
$\mathrm{Log}X$	Operator to map directly the vector space with X.
$\|X\|$ or $\|X\|_2$	Operator norm of matrix X.
$\|X\|_F$	Frobenius norm of matrix X.
	Note: Unmarked units adhere to international standard definitions.

I. INTRODUCTION

DIABETES is estimated to affect approximately 530 million adults worldwide, with a global prevalence of 10.5% among adults aged 20–79 years based on surveys in [1] and [2]. Generally, diabetes can be categorized into Type 1 Diabetes mellitus (T1DM), Type 2 Diabetes mellitus (T2DM), and gestational diabetes. Among these, T2DM is known as adult-onset diabetes or late-onset diabetes mellitus as it occurs in late life, which, notably, accounts for 90%–95% of people diagnosed [3], [4]. Treatments for T2DM begin with lifestyle management, followed by pharmacologic treatment and surgical therapy, if indicated. Common surgical procedures include: Roux-en-Y gastric bypass [5], sleeve gastrectomy [6], laparoscopic adjustable gastric banding [7], magnetic-assisted method—magnetic compression anastomosis (MCA) [8]. Compared to the former therapy methods, MCA, as a promising advancement, offers a minimally invasive alternative since its recanalization of disconnected tracts with upsides in minimally invasive, reduced complications, and precision alignment [9]. Benefiting from these advantages, its application is pervasive

Received 3 March 2025; revised 31 July 2025; accepted 19 September 2025. Date of publication 12 November 2025; date of current version 8 January 2026. This work was supported in part by the Hong Kong Research Grant Council under Project C4042-23GF, Project 14214322, Project 14200623, and Project 14206325. This article was recommended for publication by Associate Editor P. Renaud and Editor A. Menciassi upon evaluation of the reviewers' comments. *(Corresponding author: Zheng Li.)*

Yichong Sun, Yitian Xian, Ruoyu Xu, Wai Shing Chan, and Hon Chi Yip are with the Department of Surgery, The Chinese University of Hong Kong, Hong Kong, China (e-mail: yichongsun@link.cuhk.edu.hk; yitianxian@link.cuhk.edu.hk; ruoyuxu@cuhk.edu.hk; waishingchan@link.cuhk.edu.hk; hcyip@cuhk.edu.hk).

Philip Wai Yan Chiu and Zheng Li are with the Department of Surgery, Chow Yuk Ho Technology Centre for Innovative Medicine, Li Ka Shing Institute of Health Science and Multi-Scale Medical Robotics Center, The Chinese University of Hong Kong, Hong Kong, China (e-mail: philipchiu@surgery.cuhk.edu.hk; lizheng@cuhk.edu.hk).

This article has supplementary downloadable material available at https://doi.org/10.1109/TRO.2025.3631817, provided by the authors.

Digital Object Identifier 10.1109/TRO.2025.3631817

IEEE Transactions on Robotics (T-RO) paper, presented at ICRA 2026, Vienna, Austria. Cite as T-RO paper.

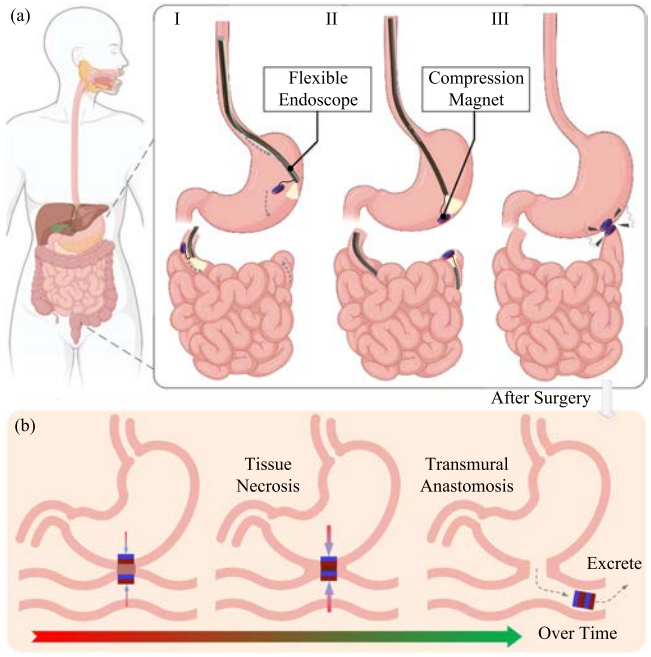

Fig. 1. Illustration of MCA surgery and anastomosis procedures in a stomach-intestine case. (a) Conceptual illustration of endoluminal MCA surgery procedure using flexible endoscopy. Two flexible endoscopes are attached with compression magnets, which are used to achieve compression in different endoluminal tracts, e.g., the stomach and intestine, as shown from subfigures I-II. A successful magnetic compression can be illustrated in subfigure III. (b) Anastomosis procedure illustration after surgery. From left to right, the side-to-side compression magnets squeeze tissue for necrosis while a new transmural anastomosis is formed until these two magnets fall off and are excreted through the natural cavity.

across digestive tracts (esophageal anastomosis for esophageal atresia, intestinal, and gastrointestinal for T2DM) [10], biliary-intestinal anastomosis for benign or severe biliary stricture [11], and pancreas-intestinal anastomosis [9].

In terms of MCA implementation, in essence, it is conducted by guiding a pair of magnets to generate attraction force between either side of the tissues that need to be jointed, as shown in an endoluminal MCA case in Fig. 1(a). These two magnets compress the tissue, leading to necrosis of the fibrotic stricture tissue and the formation of a new transmural anastomosis [12] as indicated in Fig. 1(b). Then, the whole device passes through the new opening and either naturally expelled through the gastrointestinal tract or endoscopically retrieved over time (taking over 18 days based on human trial cases in intestinal anastomosis [13]). Such a method allows less need for open surgery or tissue injury, natural healing and fusion of disconnected tracts, and accurate alignment of the puncture wound ensured by the side-to-side compression magnets. Nevertheless, these benefits for patients bring about the challenge that the surgeons need to have a good command of guiding a pair of magnets via flexible endoscopes and further placing them on, especially, in vivo either side of two disconnected endoluminal tracts. Although the endoscopes can provide an in vivo visualization, the issue of not being able to see each other's magnets via endoscopic image burdens the operations of delivering the compression magnets onto the target positions, not to mention the intricate maneuver of passing through these unstructured and narrow endoluminal tracts. As a result, surgeons have to control the compression magnets based on their experience or estimation, which leads to prolonged operative time and low procedural efficiency to some extent, thereby necessitating feedback via open surgery or invasive laparoscopic methods that create surgical wound [13], [14]. Compared to open surgery or invasive approaches that provide feedback, developments in in vivo localization of compression magnets within unstructured endoluminal tracts offer a superior pathway to achieve minimally invasive MCA surgery.

Regarding in vivo localization techniques for medical devices, several clinically established schemes exist, such as magnetic resonance imaging (MRI) [15], medical ultrasound [16], X-ray fluoroscopy [17], and so on [18]. Nevertheless, not all the schemes are available or applicable for specific surgery. As for the MCA surgery, MRI is clearly infeasible due to the incompatibility of compression magnets with high-field environments (0.2–3.0T). Ultrasound imaging is affected by endoluminal air artifacts [19], and echogenic interference [20] from metallic compression magnets, which creates significant acoustic shadowing, blocking the ultrasound waves and obscuring views of the structures. As for X-ray fluoroscopy, while offering a potential solution for in vivo information feedback, its clinical utility in MCA surgery is limited by challenges in acquiring real-time, full-pose data for dual compression magnets. In technical terms, general X-ray fluoroscopy suffers from inherent depth ambiguity and lacks out-of-plane rotational data in 2-D imaging [21]. Although advanced computer vision methods can estimate single-object poses through preliminary data acquisition and model training [22], their scalability to scenarios involving multiple objects, such as dual compression magnets, remains understudied. Additionally, the harmful radiation from real-time X-ray imaging systems [23], coupled with the need for surgeons to remain beside the operating table to handle flexible endoscopes [24], substantially reduces their practicality and acceptance among surgeons to a degree. Collectively, open surgery or laparoscopic procedure causes invasive incisions, while fluoroscopy involves radiation exposure and cannot directly provide essential information. These drawbacks reveal a critical gap in MCA surgery navigation: the need for a nonsurgical wound (NSW) and radiation-free (RF) method providing real-time in vivo information.

Building upon this analysis, a consideration is proposed regarding whether the intrinsic magnetic field can be leveraged to acquire localization information (without adding onboard electronics to the compression magnets), given that compression magnets are already present within the body during MCA surgery as magnetic field sources. This approach, referred to as magnetic localization [25], can be performed to further calculate in vivo device pose information in real-time, thereby satisfying surgeons' requirements of standing by the surgical bed with no risk of radiation while manipulating the endoscope. In fact, many profound works have been developed to localize in vivo magnetic devices using the magnetic localization approach. For example, magnetic sensors array scheme is proposed to conduct real-time infra-body localization based on the measurement of the magnetic field generated by the magnetic devices [25], [26], [27]. Critically, however, these existing methods primarily address single-object localization while directly applying these

IEEE Transactions on Robotics (T-RO) paper, presented at ICRA 2026, Vienna, Austria. Cite as T-RO paper.

methods to MCA surgery is problematic because it involves two compression magnets moving simultaneously within the measurement space—a multiple magnets scenario. About the research in multimagnetic localization, albeit pieces of literature investigated magnetic localization for multiobjects [28], [29], it only shows that the magnetic localization results in three-DoF or five-DoF information calculation. Whereas our scheme aims to utilize six-DoF information, that is $\mathbb{SE}(3)$ information, for further guiding interaction. Consequently, current research lacks reliable methods for full-DoF localization of multiple magnets. This underscores the need for further investigation to meet the specific demands of MCA surgery.

Beyond overcoming in vivo multimagnetic localization, effective interfacing remains critical for clinical adoption. Surgeons require intuitive feedback to leverage device pose information during procedures. In digestive MCA surgery, for example, operators manipulate flexible endoscopes while focusing primarily on the endoscopic monitor, making direct integration of guidance cues into this visual channel essential to avoid context switching or distraction. This motivates that instead of using the other views to showcase the $\mathbb{SE}(3)$ information only, it is more reasonable to render this information onto the original endoscopic visualization so that the surgeons can stay informed and focused, minimizing distractions and providing a seamless experience. A similar concept has been proposed by researchers, known as head-up display (HUD) [30] (viewing information with the head positioned "up" and looking forward), which has been productively applied as an assistant system in various domains [31], [32]. In recent years, the integration of HUD or similar technology has expanded into medical applications, particularly in minimally invasive surgery [33], [34], [35]. By providing real-time visualization of critical parameters such as guiding overlays, instrument positioning, and surgery data, HUD systems offer surgeons intuitive guidance during complex procedures. However, integrating HUDs into MCA surgical environments poses unique challenges that demand specialized frameworks tailored to surgical workflows. These include compression magnets location and force estimation, real-time endoscopic image processing, and seamless hardware-software integration. Given the current state of research, a significant gap remains in addressing these clinical needs in endoluminal MCA surgery.

Based on the above discussion, it is concluded: 1) existing in vivo feedback modalities fail to satisfy the dual imperatives of NSW and RF operation for endoluminal MCA surgery; 2) while magnetic localization offers a promising NSW/RF-compatible approach for magnets' localization, current implementations lack reliable full-pose localization for multiple magnets in MCA surgery case; 3) even with accurate compression magnets' location and force information, no intuitive guidance interface exists to translate complex spatial relationships into actionable feedback within the surgeon's endoscopic workflow, impeding clinical adoption. To overcome the aforementioned challenges, this study introduces the MagsL-HUD endoscopic system framework designed to enable intuitive MCA surgery in unstructured endoluminal environments. This innovative approach combines multimagnetic six-DoF localization with an endoscopic HUD strategy, offering precise spatial guidance and intuitive visualization tailored to the unique demands of endoluminal MCA procedures. The key contributions of this research are as follows.

1) To the best of the author's knowledge, this work is the first to propose the MagsL-HUD endoscopic system for MCA surgery in unstructured endoluminal environments. This framework tackles key challenges, including the absence of NSW/RF-compatible localization feedback, limited informational guidance, and the heavy reliance on the surgeon's experience.
2) It designed a novel Endo-MagCap as a standard device with a hold/fire mechanism and presented an optimization-based multimagnetic six-DoF localization algorithm with adaptive solution spaces. Together, these methods enable controllable firing deployment and six-DoF localization feedback of two compression magnets.
3) It successfully conducted a proof-of-concept test in porcine ex vivo endoluminal MCA surgery, where the system demonstrated its ability to perform a stomach-colon MCA procedure. These results serve as a reference for future clinical analyses and translation.

The rest of this article is organized as follows. Section II presents the systematic framework and development. Section III details the methodology for implementing multimagnetic six-DoF localization and endoscopic HUD synchronization. Moreover, quantitative and qualitative experimental validation is provided in Section IV. Finally, Section V concludes this article. Up to here, it first provides the notation in Nomenclature for understanding and rigour of the mathematical methods presented in this article.

II. Conceptual Framework and Development of MagsL-HUD Endoscopic System

In this section, the overall conceptual framework of the MagsL-HUD endoscopic system is proposed. Besides, a detailed design approach for the proposed Endo-MagCap device is presented.

A. MagsL-HUD Endoscopic System Framework

The proposed MagsL-HUD endoscopic system framework is illustrated in Fig. 2, which mainly comprises three parts: data feedback from the clinical setting, multimagnetic six-DoF localization and HUD information fusion, and intuitive interface output.

1) Data Feedback: For the data collection procedure, as indicated in Fig. 2, there are two flexible endoscopes with an Endo-MagCap device (details seen in Section II-B) and a magnetic localization system at the hardware layer. First, the endoscopes are deployed in the same way as the general endoluminal MCA surgery. Two endoscopes are inserted from orifices to enter different endoluminal tracts. Then, the EVs are collected for further imaging fusion. Besides, the self-developed magnetic localization system is mounted on the surgical bed. In this article, the multimagnetic localization system is designed based on the magnetic sensor array approach. The key component of the multimagnetic localization system is the planar magnetic sensor

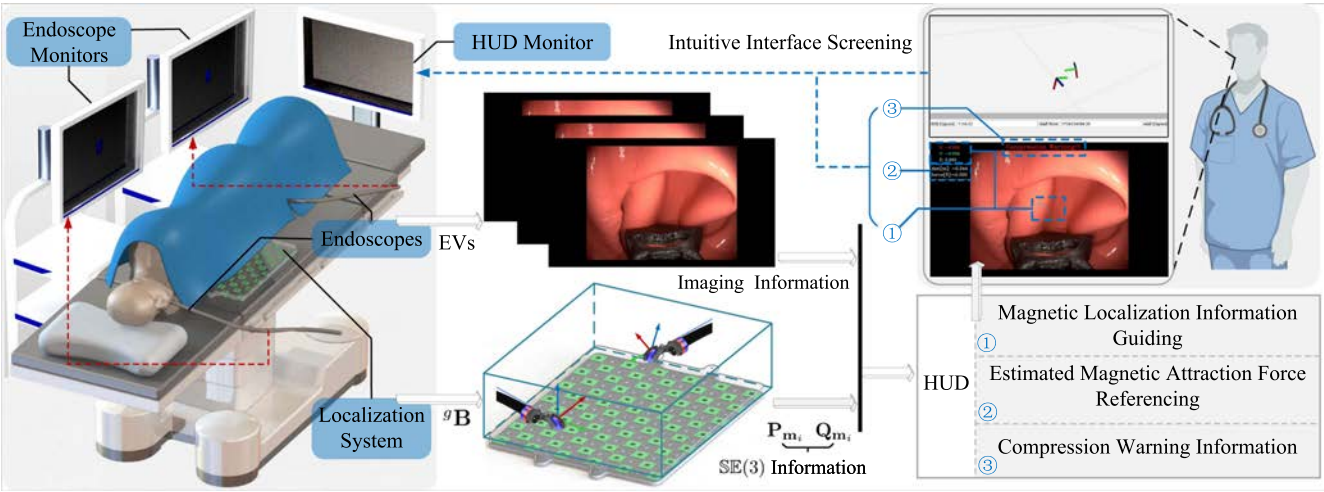

Fig. 2. Overall framework of the MagsL-HUD endoscopic system for endoluminal MCA surgery and its workflow. The patient lies on the surgical bed which is equipped with a magnetic localization system (magnetic sensor array) to detect the magnetic field for further calculating $\mathbb{SE}(3)$ information of two compression magnets via proposed multimagnetic six-DoF localization algorithm. Two endoscopes are inserted from different orifices to get into complex endoluminal tracts and deliver the proposed Endo-MagCap device under the guidance of HUD information from magnetic localization and endoscopic images. With the intuitive interface screening on the HUD monitor, the surgeons handle the endoscope and control the Endo-MagCap device to fire the compression magnets to achieve complete MCA surgery in unstructured endoluminal environments.

array, distributed as shown in Figs. 2 and 4. When the surgery is conducted, the magnetic localization system measures the magnetic field $^{g}\mathbf{B}$ as defined in (10), generated by the magnets of the Endo-MagCap device inside the endoluminal environments. The magnetic field data are collected for the subsequent execution of the multimagnetic six-DoF localization algorithm.

2) MagsL-HUD Fusion: Mainly in the software layer, the multimagnetic six-DoF localization algorithm is performed based on the magnetic field data collected in the first procedure, which provides the poses of the compression magnets, that is $\mathbb{SE}(3)$ information ($\mathbf{P}_{\mathbf{m}_i}$ in position $\mathbf{Q}_{\mathbf{m}_i}$ in orientation, details seen Section III-C). Meanwhile, the magnets' $\mathbb{SE}(3)$ information is treated as one of the inputs for the fusion with the EVs data collected in the first procedure to offer HUD visualization. The HUD information is comprised of localization-based information guidance, estimated magnetic attraction force referencing, and compression warnings. All this information is derived based on the magnets' $\mathbb{SE}(3)$ information and the surgeons' suggestions, as well as the experience gained during the development process. Besides, the hardware for this part is mainly a computer.

3) Intuitive Interface Outputs: Intuitive interface output is designed as the final step of the MagsL-HUD endoscopic system framework, which is expected to provide both the HUD intuitive guiding and reference as well as warning, based on the original EVs. As illustrated in Fig. 2 and more detailed in Fig. 5, two interface screenings are displayed. The first interface screening is the multimagnetic six-DoF localization results built in a simulator environment by using a coordinate axis. In addition, the HUD information is rendered into the original EVs. The final rendering images are treated as the second interface screening to achieve an intuitive visualization of the other compression magnet and guidance of the Endo-MagCap device. Both interface screenings are outputted on a medical monitor as an HUD monitor.

It is worth noting that the proposed MagsL-HUD endoscopic system addresses the significant challenge of localizing in vivo compression magnets while improving the synergy between the surgeon and the system. On the one hand, the MagsL-HUD strategy leverages the inherent magnetic field of the compression magnets, eliminating the need for additional active onboard devices and ensuring patient safety. Additionally, it fully considers the surgeon's operating habits of focusing on EVs' visualization and facilitates the seamless integration of magnetic localization information.

Moreover, it is evident that the implementation of MCA surgery finally requires successful compression, which requires a delivery device design with specialized configuration and functionality for the compression magnets attached to the endoscopes. This necessity drives the development of the novel Endo-MagCap device design, which is discussed in detail in the following subsection.

B. Endo-MagCap Device Design for Endoluminal MCA

The target here is to develop the Endo-MagCap device with the configuration for six-DoF localization and the functionality in the hold/fire mechanism for the compression magnets.

1) Magnets Configuration in Endo-MagCap: In this article, the designed Endo-MagCap consists of two orthogonal magnets. As shown in Fig. 3(d), a localization magnet, that is, a magnet ring, is put on the 3-D printed connector which is designed with a mounting hole to be inserted into the end of the endoscope. Besides, the compression magnet is put on the tip of the 3-D-printed connector. Generally, in MCA surgery, there are two compression magnets with magnetic dipole moment defined as $\mathbf{m}_i \in \mathbb{R}^3$ ($i \in \mathbb{N}^+$ takes values in set $\mathbb{C}_{mag} = \{1, 2\}$). For each i-th compression magnet, there is a localization magnet with magnetic dipole moment defined as $\mathbf{L}_i \in \mathbb{R}^3$. Then, the

IEEE Transactions on Robotics (T-RO) paper, presented at ICRA 2026, Vienna, Austria. Cite as T-RO paper.

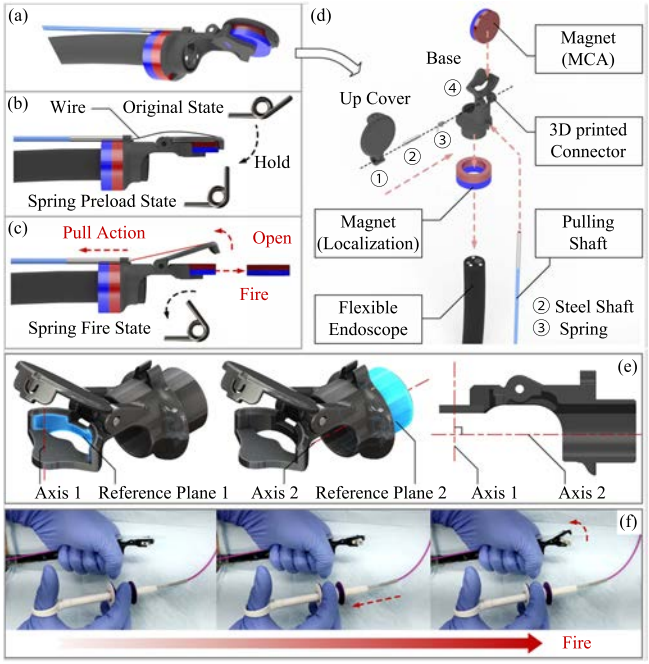

Fig. 3. Conceptual illustration and implementation of the Endo-MagCap device. (a) Illustration of the Endo-MagCap device mounted onto the tip of the flexible endoscopes. (b) Illustration of the Endo-MagCap device in the hold state. (c) Illustration of the Endo-MagCap device in a fire state. (d) Exploded-view drawing about the mechanical design of the Endo-MagCap device. (e) Illustration of the 3-D-printed connector design for orthogonal mounting. (f) Working flow for using the Endo-MagCap (Surgeons pull the shaft to open the up the cover, firing the magnet).

following constraint holds:

$$\mathbf{m}_i \cdot \mathbf{L}_i = 0, \quad \forall i \in \mathbb{C}_{\text{mag}}. \tag{1}$$

To ensure orthogonal mounting, as shown in Fig. 3(e), the 3-D-printed connector incorporates two reference surfaces: Reference Plane 1 aligns the first magnet's moment with Axis 1 using a locating slot and spring-loaded upper cover to secure it without rotation; Reference Plane 2, a perpendicular mounting shaft surface, aligns the second magnet's moment with Axis 2 via an interference fit. The orthogonality between Axis 1 and Axis 2 is inherently guaranteed by the monolithic connector design. Such a design makes sure that the distribution of the combined magnetic field is not axis-symmetric but anisotropic, which satisfies the need for six-DoF localization.

2) Compression Magnets Hold/Fire Mechanism: The other function of the Endo-MagCap device is to deliver the compression magnet as clinical requirements [11]. As illustrated in Fig. 3(a)–(c), there are 3-D-printed up cover which is connected to the base (3-D-printed Connector) by using a spring and steel shaft to allow opening and closing to hold and fire the compression magnet, respectively. Notably, the holding force is introduced by bending the spring from the original state to the preloaded state, as shown in Fig. 3(b). Moreover, a pulling shaft is attached along the endoscopic shaft to pull the wire that is tied onto the end of the up cover as indicated in Fig. 3(b) and (d). Per surgeon feedback, this pulling design is consistent with traditional fire equipment in endoscopic surgery (e.g., endoscopic tractor), making it easier to learn and operate. The working flow illustration of the Endo-MagCap device is indicated in Fig. 3(f). When the surgeon decides to fire the compression magnet, they can pull the pulling shaft to open up cover so that the compression magnet can be released, attaching to the other magnet on the other endoluminal tracts. More mechanical analysis can be found in Appendix A.

The Endo-MagCap design is now complete, forming the foundation for the detailed techniques of multimagnetic six-DoF localization, which are presented in the following section.

III. Multimagnetic Six-DoF Localization and HUD Harmonizing Scheme

This section focuses on the detailed technique discussion on multimagnetic six-DoF localization using the magnetic sensor array approach and synchronizing the HUD scheme based on magnetic localization information.

A. Coordinate Systems Definition and Transformation

As shown in Fig. 4(a), there are $m \times n$ magnetic sensors, which are distributed on the sensor pad with $\forall m,\ n \in \mathbb{N}^+$. For each sensor, the corresponding located frame coordinate is defined as ${}^{(m,n)}\mathcal{O}$. Besides, the global frame coordinate ${}^{g}\mathcal{O}$ is defined at the geometric center on the surface of the magnetic sensor pad. Based on the above definitions, the transformation between ${}^{(m,n)}\mathcal{O}$ and ${}^{g}\mathcal{O}$ can be defined as ${}^{g}\mathrm{T}_{(m,n)} \in \mathbb{SE}(3)$ with $\mathbf{R}_{(m,n)} \in \mathbb{SO}(3)$ and $\mathbf{P}_{(m,n)} \in \mathbb{R}^3$ being the rotation matrix and position vector of (m,n) magnetic sensor relative to ${}^{g}\mathcal{O}$. Next, define the frame coordinate systems ${}^{\mathbf{m}_i}\mathcal{O}$ for the i-th compression magnet with the origin at the geometric center of the magnet, where $i \in \mathbb{C}_{mag}$. The transformation between ${}^{\mathbf{m}_i}\mathcal{O}$ and ${}^{g}\mathcal{O}$ can be defined as ${}^{g}\mathrm{T}_{\mathbf{m}_i} \in \mathbb{SE}(3)$ with $\mathbf{R}_{\mathbf{m}_i} \in \mathbb{SO}(3)$ and $\mathbf{P}_{\mathbf{m}_i} \in \mathbb{R}^3$ being the rotation matrix and the position vector of compression magnets relative to ${}^{g}\mathcal{O}$.

Moreover, for each compression magnet, there is a localization magnet with frame coordinate ${}^{\mathbf{L}_i}\mathcal{O}$ with the origin in the geometry center of magnet. The known transformation between ${}^{\mathbf{L}_i}\mathcal{O}$ and ${}^{\mathbf{m}_i}\mathcal{O}$ can be defined as ${}^{\mathbf{m}_i}\mathrm{T}_{\mathbf{L}_i} \in \mathbb{SE}(3)$ with ${}^{\mathbf{m}_i}\mathbf{R}_{\mathbf{L}_i} \in \mathbb{SO}(3)$ and ${}^{\mathbf{m}_i}\mathbf{P}_{\mathbf{L}_i} \in \mathbb{R}^3$ being the rotation matrix and the position vector of the localization magnets regarding compression magnets. Especially, ${}^{\mathbf{m}_i}\mathbf{R}_{\mathbf{L}_i}$ is designed in a specific format, that is, the vector $\mathbf{m}_i$ and $\mathbf{L}_i$ are orthogonal, as defined in (1), for the further achievement of six-DoF localization of the Endo-MagCap devices. Before that, the magnetic model should be presented as preliminary.

B. Magnetic Modeling for Endo-MagCap Device

The conduction of the multimagnetic six-DoF localization algorithm is based on the measured magnetic field generated by the compression and localization magnets. First, as indicated in Fig. 4(a), assume the i-th compression magnet in the Endo-MagCap is located in position $\mathbf{P}_{\mathbf{m}_i} \in \mathbb{R}^3$, regarding to the global frame coordinate ${}^{g}\mathcal{O}$. Since that in most cases, the Euclidean distance of $\mathbf{P}_{\mathbf{m}_i}$ is bigger than the radius of the magnets in the Endo-MagCap, the magnetic field in each (m,n)

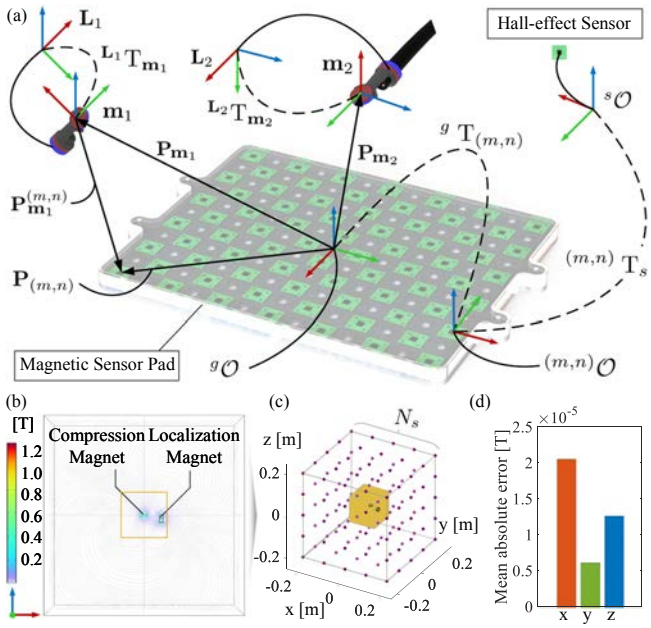

Fig. 4. Illustration of coordinate systems in magnetic localization system and simulation results. (a) Illustration of coordinate systems for magnets in Endo-MagCap and magnetic sensor pad as well as magnetic sensor and other parameters. (b) Magnetic field distribution of magnets in Endo-MagCap by using FEM simulations. (c) Illustration of the sampling points for magnets in Endo-MagCap. (d) Magnetic field modeling MAE results in axes.

magnetic sensor, generated by the i-th compression magnet can be approximately modeled as the magnetic dipole model [36] with respect to $\mathbf{P}_{\mathbf{m}_i}^{(m,n)}$ and $\mathbf{m}_i$ as follows:

$$\mathbf{B}\left(\mathbf{P}_{\mathbf{m}_i}^{(m,n)}, \mathbf{m}_i\right) = \left[\frac{\mu_0\left(3\hat{\mathbf{P}}_{\mathbf{m}_i}^{(m,n)}\hat{\mathbf{P}}_{\mathbf{m}_i}^{(m,n)\top} - \mathbb{I}_{3\times 3}\right)}{4\pi\left\|\mathbf{P}_{\mathbf{m}_i}^{(m,n)}\right\|^3}\right]\mathbf{m}_i \in \mathbb{R}^3 \tag{2}$$

with the following:

$$\hat{\mathbf{P}}_{\mathbf{m}_i}^{(m,n)} = \mathbf{P}_{\mathbf{m}_i}^{(m,n)} / \left\|\mathbf{P}_{\mathbf{m}_i}^{(m,n)}\right\|, \mathbf{P}_{\mathbf{m}_i}^{(m,n)} = \mathbf{P}_{(m,n)} - \mathbf{P}_{\mathbf{m}_i}$$

where $\mathbf{P}_{(m,n)}$ are prior known and μ_0 is the vacuum permeability constant. By aligning $\mathbf{m}_i$ with x-axis with axis unit $\hat{x} = [1\ 0\ 0]^\top$, it can be inferred as

$$\mathbf{m}_i = \|\mathbf{m}_i\|\ \mathbf{R}_{\mathbf{m}_i}\ \hat{x} \tag{3}$$

where $\|\mathbf{m}_i\|$ is the constant magnetic moment magnitude for the i-th compression magnet. It is worth mentioning that $\|\mathbf{m}_i\|$ are the inherent attributes when the configuration and size of the compression magnets are confirmed by surgeons. Likewise, the magnetic field generated by the localization magnets can be represented as

$$\mathbf{B}\left(\mathbf{P}_{\mathbf{L}_i}^{(m,n)}, \mathbf{L}_i\right) = \left[\frac{\mu_0\left(3\hat{\mathbf{P}}_{\mathbf{L}_i}^{(m,n)}\hat{\mathbf{P}}_{\mathbf{L}_i}^{(m,n)\top} - \mathbb{I}_{3\times 3}\right)}{4\pi\left\|\mathbf{P}_{\mathbf{L}_i}^{(m,n)}\right\|^3}\right]\mathbf{L}_i \in \mathbb{R}^3 \tag{4}$$

with the following:

$$\hat{\mathbf{P}}_{\mathbf{L}_i}^{(m,n)} = \mathbf{P}_{\mathbf{L}_i}^{(m,n)} / \left\|\mathbf{P}_{\mathbf{L}_i}^{(m,n)}\right\|, \mathbf{P}_{\mathbf{L}_i}^{(m,n)} = \mathbf{P}_{(m,n)} - \mathbf{P}_{\mathbf{L}_i}$$

where there exists $[\mathbf{P}_{\mathbf{L}_i}^\top\ 1]^\top = {}^g\mathrm{T}_{\mathbf{m}_i}\ [{}^{\mathbf{m}_i}\mathbf{P}_{\mathbf{L}_i}^\top\ 1]^\top$, which further infers

$$\mathbf{P}_{\mathbf{L}_i} = \mathbf{R}_{\mathbf{m}_i}\ {}^{\mathbf{m}_i}\mathbf{P}_{\mathbf{L}_i} + \mathbf{P}_{\mathbf{m}_i}. \tag{5}$$

Then, with the help of (3) and known transformation ${}^{\mathbf{m}_i}\mathrm{T}_{\mathbf{L}_i}$, $\mathbf{L}_i$ can be explicitly expressed as

$$\mathbf{L}_i = \|\mathbf{L}_i\|\ \frac{\mathbf{m}_i}{\|\mathbf{m}_i\|}\ {}^{\mathbf{m}_i}\mathbf{R}_{\mathbf{L}_i} = \|\mathbf{L}_i\|\ \mathbf{R}_{\mathbf{m}_i}\ {}^{\mathbf{m}_i}\mathbf{R}_{\mathbf{L}_i}\ \hat{x}. \tag{6}$$

It can be observed that in magnetic model (4), $\mathbf{L}_i$ and $\mathbf{P}_{\mathbf{L}_i}^{(m,n)}$ are dependent on variables $\mathbf{R}_{\mathbf{m}_i}$ and $\mathbf{P}_{\mathbf{m}_i}$ respectively and the other parameters are known. Also, $\mathbf{m}_i$ and $\mathbf{P}_{\mathbf{m}_i}^{(m,n)}$ in (2) are dependent on variables $\mathbf{R}_{\mathbf{m}_i}$ and $\mathbf{P}_{\mathbf{m}_i}$ since $\|\mathbf{m}_i\|$ and $\mathbf{P}_{(m,n)}$ are given. Therefore, the combined magnetic field in (m,n) magnetic sensor can be written as

$$\mathbf{f}\left(\mathbf{P}_{\mathbf{m}_i}^{(m,n)}, \mathbf{R}_{\mathbf{m}_i}\right) = \mathbf{B}\left(\mathbf{P}_{\mathbf{m}_i}^{(m,n)}, \mathbf{m}_i\right) + \mathbf{B}\left(\mathbf{P}_{\mathbf{L}_i}^{(m,n)}, \mathbf{L}_i\right) \tag{7}$$

which is actually dependent in $\mathbf{R}_{\mathbf{m}_i}$ and $\mathbf{P}_{\mathbf{m}_i}$ based on the derivation in (5) and (6) where $\mathbf{P}_{(m,n)}$ are known condition.

In order to assess the modeling accuracy of the combined magnetic field based on the magnetic dipole models (2) and (4), the finite element method (FEM) is used to obtain the simulated magnetic field for the magnets in the Endo-MagCap, as illustrated in Fig. 4(b). A real-size magnet model like the magnets configuration in Endo-MagCap is built up in FEM simulation.[1] For accuracy evaluation, the mean absolute error (MAE) as described in [37] is used by

$$\mathrm{MAE} = \frac{1}{N}\sum_{s=1}^{N} \mid o_s - \hat{o}_s \mid \tag{8}$$

where o_s and $\hat{o}_s$ are the magnetic field componentwise via FEM method and its corresponding results via (7), respectively. The sampling space consisted of a cube of size 0.4m. For brevity, it denotes a grid of size N_s =100, excluding points in the near-field space, defined as cube space with side length as 0.12 m as shown the inner golden box in Fig. 4(c). Then, the total sampling number N =973000. Finally, by using (8), the MAE in x-, y-, and z-axes are obtained as 2.0618×10^{-5} T, 6.2340×10^{-6} T, and 1.2729×10^{-5} T, respectively, as illustrated in Fig. 4(d). Taking FEM as the reference standard, the modeling accuracy can reach MAE below 3×10^{-5} T for each axis in our permanent magnets case. It is recognized that the final localization accuracy is influenced not only by modeling errors but also by sensor noise [38] and algorithm scheme [39]. The overall localization performance will be evaluated in subsequent experimental validation. For a detailed analysis of modeling accuracy, refer to the comprehensive study in [37].

Next, based on the above magnetic field model analysis and discussion, the localization algorithm is derived in the following subsection.

[1]FEM model is available as a multimedia attachment with this article.

IEEE Transactions on Robotics (T-RO) paper, presented at ICRA 2026, Vienna, Austria. Cite as T-RO paper.

C. Multimagnetic Six-DoF Localization With Adaptive Solution Space

Assume that the magnetic field measured by $(m,\ n)$ sensor is $\mathbf{M}_{(m,n)} \in \mathbb{R}^3$. Noting that $\mathbf{M}_{(m,n)}$ is the raw signal data with respect to inner sensor frame coordinate ${}^{s}\mathcal{O}$. The known transformation relation between ${}^{(m,n)}\mathcal{O}$ and ${}^{s}\mathcal{O}$ is given as ${}^{(m,n)}\mathrm{T}_s \in \mathbb{SE}(3)$ which extracts related rotation matrix ${}^{(m,n)}\mathbf{R}_s \in \mathbb{SO}(3)$. Based on this information, the magnetic field ${}^{g}\mathbf{M}_{(m,n)} \in \mathbb{R}^3$ for each (m,n) magnetic sensor with respect to ${}^{g}\mathcal{O}$ can be obtained by

$$ {}^{g}\mathbf{M}_{(m,n)} = \mathbf{R}_{(m,n)}\ {}^{(m,n)}\mathbf{R}_s\ \mathbf{M}_{(m,n)}. \tag{9} $$

With the introduction of (2) and (9), the multimagnetic localization method is formulated as an optimization problem. Initially, using (9), the measured magnetic field at the (m,n) magnetic sensors can be represented in a compact matrix as

$$ {}^{g}\mathbf{B} = \begin{bmatrix} {}^{g}\mathbf{M}_{(1,1)} & \cdots & {}^{g}\mathbf{M}_{(1,n)} \\ \vdots & \ddots & \vdots \\ {}^{g}\mathbf{M}_{(m,1)} & \cdots & {}^{g}\mathbf{M}_{(m,n)} \end{bmatrix}_{3m\times n}. \tag{10} $$

Besides, based on the combined magnetic model (7), the nominal magnetic field generated by i-th Endo-MagCap can be constructed as

$$ \bar{\mathbf{B}}\left(\mathbf{P}_{\mathbf{m}_i}, \mathbf{R}_{\mathbf{m}_i}\right) = \begin{bmatrix} \mathbf{f}\left(\mathbf{P}_{\mathbf{m}_i}^{(1,1)}, \mathbf{R}_{\mathbf{m}_i}\right) & \cdots & \mathbf{f}\left(\mathbf{P}_{\mathbf{m}_i}^{(1,n)}, \mathbf{R}_{\mathbf{m}_i}\right) \\ \vdots & \ddots & \vdots \\ \mathbf{f}\left(\mathbf{P}_{\mathbf{m}_i}^{(m,1)}, \mathbf{R}_{\mathbf{m}_i}\right) & \cdots & \mathbf{f}\left(\mathbf{P}_{\mathbf{m}_i}^{(m,n)}, \mathbf{R}_{\mathbf{m}_i}\right) \end{bmatrix}. \tag{11} $$

Subsequently, it is observed that when calculating the six-DoF information for the i-th Endo-MagCap, the variables $\mathbf{R}_{\mathbf{m}_i}$ are defined on the $\mathbb{SO}(3)$ manifold. To simplify the optimization calculation, this article introduces a transformation from $\mathbb{SO}(3)$ to $\mathbb{H}$, reducing the number of variables in the optimization function. First, define the solution variables for the i-th Endo-MagCap as

$$ \mathbf{x}_i = \begin{bmatrix} \mathbf{P}_{\mathbf{m}_i}^{\top} & \mathbf{Q}_{\mathbf{m}_i}^{\top} \end{bmatrix}^{\top} \in \mathbb{R}^7 $$

where $\mathbf{Q}_{\mathbf{m}_i} = [q_w\ q_x\ q_y\ q_z]^{\top} \in \mathbb{H}$ with the normalized condition $q_w^2 + q_x^2 + q_y^2 + q_z^2 = 1$. Then, the nominal magnetic field (11) can be represented as $\bar{\mathbf{B}}(\mathbf{P}_{\mathbf{m}_i}, \mathbf{Q}_{\mathbf{m}_i})$ together with the following definition [40]:

$$ \mathbf{R}_{\mathbf{m}_i} = \begin{bmatrix} 1-2(q_y^2+q_z^2) & 2(q_xq_y - q_wq_z) & 2(q_xq_z + q_wq_y) \\ 2(q_xq_y + q_wq_z) & 1-2(q_x^2+q_z^2) & 2(q_yq_z - q_wq_z) \\ 2(q_xq_z - q_wq_y) & 2(q_yq_z + q_wq_z) & 1-2(q_x^2+q_y^2) \end{bmatrix}. \tag{12} $$

Using the definitions in (10) and (11), along with the conversion in (12), the optimization function for the magnetic localization algorithm can be formulated as follows:

$$ f(\mathbf{P}_{\mathbf{m}_i}, \mathbf{Q}_{\mathbf{m}_i}) = \left\| {}^{g}\mathbf{B} - \sum_{i\in\mathbb{C}_{mag}} \bar{\mathbf{B}}\left(\mathbf{P}_{\mathbf{m}_i}, \mathbf{Q}_{\mathbf{m}_i}\right) \right\|_F \tag{13} $$

which can further infer $\mathbf{x}_i$ by solving

$$ \mathbf{x}_i = \arg \min_{\mathbf{P}_{\mathbf{m}_i}\in\mathbb{R}^3, \mathbf{Q}_{\mathbf{m}_i}\in\mathbb{H}} f(\mathbf{P}_{\mathbf{m}_i}, \mathbf{Q}_{\mathbf{m}_i}). \tag{14} $$

In a practical implementation of (14), it is observed that the conditions $\mathbf{P}_{\mathbf{m}_i} \in \mathbb{R}^3$ and $\mathbf{Q}_{\mathbf{m}_i} \in \mathbb{H}$ result in an ample solution space, which compromises both robustness and computational efficiency. To address this issue, this article proposes an adaptive solution space method to improve the efficiency of multimagnetic six-DoF localization. The approach begins by defining a workspace as

$$ \mathbb{S}_{work} = \left\{ \mathbf{P} \in \mathbb{R}^3 \middle| \underline{\mathbf{P}} \preceq \mathbf{P} \preceq \overline{\mathbf{P}} \right\} \tag{15} $$

where $\underline{\mathbf{P}}, \overline{\mathbf{P}} \in \mathbb{R}^3$ are the lower and upper bounds, respectively. For elapsed time $\Delta t(k) \in \mathbb{R}^+$ from $t(k-1)$ to $t(k)$ moment, $k \in \mathbb{N}$, the velocities for i-th Endo-MagCap can be defined as

$$ \begin{cases} \mathbf{V}_{i,k} = \left[\mathbf{P}_{\mathbf{m}_i,k} - \mathbf{P}_{\mathbf{m}_i,k-1}\right] / \Delta t(k) \\ \boldsymbol{\omega}_{\mathbf{m}_i,k} = 2\theta_k / \Delta t(k)\ \mathbf{u} \end{cases} \tag{16} $$

Algorithm 1: Multimagnetic Six-DoF Localization Algorithm.

Input: Magnetic field data ${}^{g}\mathbf{B}$;
Output: $\mathbf{P}_{\mathbf{m}_i}$ and $\mathbf{Q}_{\mathbf{m}_i}$ for i-th Endo-MagCap;
initialize $k = 0$, $\mathbf{P}_{\mathbf{m}_i,0} = \mathbf{P}_{\mathbf{m}_i,int}$ and $\mathbf{Q}_{\mathbf{m}_i,0} = \mathbf{Q}_{\mathbf{m}_i,int}$;
initialize solution spaces $\mathbb{S}_{\mathbf{P}_{\mathbf{m}_i}} = \mathbb{S}_{work}$, $\mathbb{S}_{\mathbf{Q}_{\mathbf{m}_i}} = \mathbb{Q}$ and parameters c_1, c_2, and c_3;
initialize steps length $K \in \mathbb{N}^+$;
while *steps* $k < K$ **do**
  Update ${}^{g}\mathbf{B}$ via (10) based on (9);
  Construct $\bar{\mathbf{B}}\left(\mathbf{P}_{\mathbf{m}_i}, \mathbf{Q}_{\mathbf{m}_i}\right)$ via (11) based on (7) and (12);
  Compute $\mathbf{P}_{\mathbf{m}_i,k}$ and $\mathbf{Q}_{\mathbf{m}_i,k}$ by solving optimization function (14) with the solution spaces $\mathbb{S}_{\mathbf{P}_{\mathbf{m}_i}}$ and $\mathbb{S}_{\mathbf{Q}_{\mathbf{m}_i}}$;
  Compute $\mathbf{V}_{i,k}$ and $\omega_{i,k}$ via (16);
  if $\|\mathbf{V}_{i,k}\| < \bar{V}$ **then**
    Compute $\mathbb{S}_{\mathbf{P}_{\mathbf{m}_i,k}}$ based on (17);
    Update $\mathbb{S}_{\mathbf{P}_{\mathbf{m}_i}} \leftarrow \mathbb{S}_{\mathbf{P}_{\mathbf{m}_i,k}} \cap \mathbb{S}_{work}$;
  else
    Update $\mathbb{S}_{\mathbf{P}_{\mathbf{m}_i}} \leftarrow \mathbb{S}_{work}$;
  if $\|\omega_{\mathbf{m}_i,k}\| < \bar{\omega}$ **then**
    Compute $\mathbb{S}_{\mathbf{Q}_{\mathbf{m}_i,k}}$ based on (18);
    Update $\mathbb{S}_{\mathbf{Q}_{\mathbf{m}_i}} \leftarrow \mathbb{S}_{\mathbf{Q}_{\mathbf{m}_i,k}}$;
  else
    Update $\mathbb{S}_{\mathbf{Q}_{\mathbf{m}_i}} \leftarrow \mathbb{H}$;
  Publish $\mathbf{P}_{\mathbf{m}_i,k}$ and $\mathbf{Q}_{\mathbf{m}_i,k}$ and let $k = k+1$;

with the following:

$$\theta_k = 2\arccos\left(\delta q_{k,1}\right), \mathbf{u} = \frac{\begin{bmatrix}\delta q_{k,2} & \delta q_{k,3} & \delta q_{k,4}\end{bmatrix}^\top}{\sqrt{\delta q_{k,2}^2 + \delta q_{k,3}^2 + \delta q_{k,4}^2}}$$

$$\delta q_k = \begin{bmatrix}\delta q_{k,1} & \delta q_{k,2} & \delta q_{k,3} & \delta q_{k,4}\end{bmatrix}^\top = \mathbf{Q}_{\mathbf{m}_i,k} \otimes \mathbf{Q}_{\mathbf{m}_i,k-1}^{-1}$$

where $\mathbf{V}_{i,k} \in \mathbb{R}^3$ and $\boldsymbol{\omega}_{\mathbf{m}_i,k} \in \mathbb{R}^3$ are position and angular velocities regarding to solution $\mathbf{x}_i^\star = (\mathbf{P}_{\mathbf{m}_i,k}, \mathbf{Q}_{\mathbf{m}_i,k})$ at k moment. Then, set the adaptive solution space as the box form

$$\mathbb{S}_{\mathbf{P}_{\mathbf{m}_i,k}} = \left\{ \mathbf{P} \in \mathbb{R}^3 \middle| \mathbf{P}_{\mathbf{m}_i,k} - \mathbf{P}_{c_1,i,k} \preceq \mathbf{P} \preceq \mathbf{P}_{\mathbf{m}_i,k} + \mathbf{P}_{c_2,i,k} \right\} \tag{17}$$

with the following:

$$\mathbf{P}_{c_1,i,k} = c_1 e^{\|\mathbf{V}_{i,k}\|}\, \boldsymbol{\upsilon}_{i,k}, \mathbf{P}_{c_2,i,k} = c_2 e^{\|\mathbf{V}_{i,k}\|}\, \boldsymbol{\upsilon}_{i,k}$$

$$\boldsymbol{\upsilon}_{i,k} = \begin{bmatrix} e^{\mathbf{V}_{i,k}(1)} & e^{\mathbf{V}_{i,k}(2)} & e^{\mathbf{V}_{i,k}(3)} \end{bmatrix}^\top \in \mathbb{R}^3$$

where c_1 and $c_2 \in \mathbb{R}^+$ are known parameters to restrict the solution space for the position. The solution space is determined by the term $\|\mathbf{V}_{i,k}\|$ which makes the solution space adaptive with respect to position velocities. Moreover, the introduction of parameters c_1, and c_2 bring the benefits that when $\|\mathbf{V}_{i,k}\| \to 0$, $\mathbf{P}_{c_1} \to c_1\, \mathbb{I}_{3\times 1}$ and $\mathbf{P}_{c_2} \to c_2\, \mathbb{I}_{3\times 1}$, which makes sure that the solution space does not collapse to the null space. Likewise, the constraint solution space on the $\mathbf{Q}_{\mathbf{m}_i}$ is defined by

$$\mathbb{S}_{\mathbf{Q}_{\mathbf{m}_i,k}} = \{ \mathbf{Q} \in \mathbb{H} | \, \mathbf{Q} = (\delta q_k)^r \otimes \mathbf{Q}_{\mathbf{m}_i,k}, r \in [-c_3, c_3] \} \tag{18}$$

where $c_3 \in \mathbb{R}^+$ is known parameter. Then, based on the introduction of (16) and the definition in (15), (17), and (18), the adaptive solution space method can be constructed as

$$\mathbb{S}_{\mathbf{P}_{\mathbf{m}_i}} = \begin{cases} \mathbb{S}_{\mathbf{P}_{\mathbf{m}_i,k}} \cap \mathbb{S}_{work}, & \text{if } \|\mathbf{V}_{i,k}\| < \bar{V} \\ \mathbb{S}_{work}, & \text{otherwise} \end{cases} \tag{19}$$

$$\mathbb{S}_{\mathbf{Q}_{\mathbf{m}_i}} = \begin{cases} \mathbb{S}_{\mathbf{Q}_{\mathbf{m}_i,k}}, & \text{if } \|\boldsymbol{\omega}_{\mathbf{m}_i,k}\| < \bar{\omega} \\ \mathbb{H}, & \text{otherwise} \end{cases} \tag{20}$$

where $\bar{V} \in \mathbb{R}^+$ and $\bar{\omega} \in \mathbb{R}^+$ are the threshold position and angular velocities, respectively. These two parameters are introduced to avoid motion mutation cases, which means that when the velocities exceed the threshold value, the solution spaces $\mathbb{S}_{\mathbf{P}_{\mathbf{m}_i}}$ and $\mathbb{S}_{\mathbf{Q}_{\mathbf{m}_i}}$ for each calculation step will be released to $\mathbb{S}_{work}$ and $\mathbb{H}$, severally. Otherwise, the solution spaces are set as real-time updated solution space via (17) and (18). Eventually, under the introduction of (19) and (20) as well as (14), the multimagnetic six-DoF localization algorithm with adaptive solution space can be formed as follows.

Multimagnetic Six-DoF Localization Algorithm With Adaptive Solution Space: With the real-time updated magnetic field data matrix ${}^g\mathbf{B}$ via (10) from the magnetic localization system in k moment and the construction of nominal magnetic field matrix $\bar{\mathbf{B}}(\mathbf{P}_{\mathbf{m}_i,k}, \mathbf{Q}_{\mathbf{m}_i,k})$ via (11) and (12) by substituting conditions (3) and (6) into (2) and (4) under the magnetic dipole model assumption, the solution $\mathbf{x}_i^\star = (\mathbf{P}_{\mathbf{m}_i,k}, \mathbf{Q}_{\mathbf{m}_i,k})$ for i-th Endo-MagCap can be obtained by solving the following optimization function:

$$\begin{aligned} \mathbf{x}_i^\star &= \arg\min f(\mathbf{P}_{\mathbf{m}_i,k}, \mathbf{Q}_{\mathbf{m}_i,k}) \\ \text{s.t.} \quad & \mathbf{P}_{\mathbf{m}_i,k} \in \mathbb{S}_{\mathbf{P}_{\mathbf{m}_i}}, \mathbf{Q}_{\mathbf{m}_i,k} \in \mathbb{S}_{\mathbf{Q}_{\mathbf{m}_i}}, (19), (20) \end{aligned} \tag{21}$$

where $\mathbf{x}_i^\star$ can be rewritten as ${}^g\mathrm{T}_{\mathbf{m}_i}$ in $\mathbb{SE}(3)$ form based on conversion (12).

To provide a clearer understanding of the proposed multimagnetic six-DoF localization algorithm, the iteration process is detailed in Algorithm 1. At this stage, by solving the proposed multimagnetic six-DoF localization algorithm, the ${}^g\mathrm{T}_{\mathbf{m}_i}$ information can be further obtained. ${}^g\mathrm{T}_{\mathbf{m}_i}$ is displayed on the first interface screening by using the coordinate axis and also serves as one of the inputs for the subsequent HUD harmonizing process.

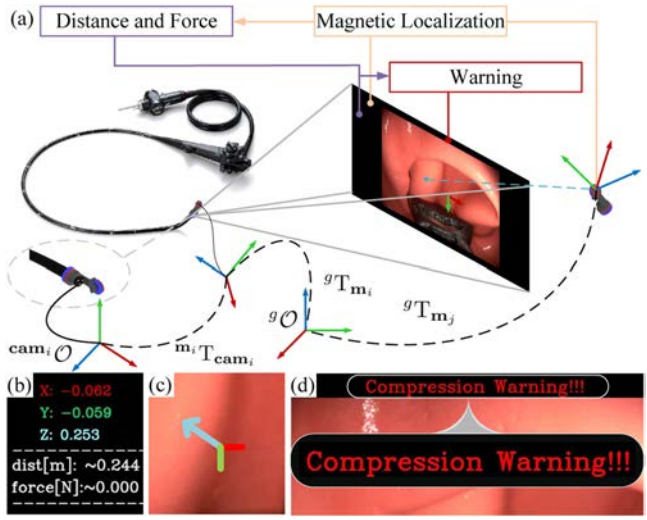

Fig. 5. Conceptual illustration of HUD integration into endoscopes and HUD information display. (a) Coordinate system definition for endoscope and HUD information indication in EVs. (b) HUD interface screening about the estimated distance and force as well as axial position in ${}^{\mathbf{cam}_i}\mathbf{P}_{\mathbf{m}_j}$. (c) HUD interface screening about moving direction guiding. (d) HUD interface screening about compression warning information and its enlarged diagram.

D. HUD Guiding for Intuitive Endoscopic Visualization

To synchronize HUD guiding information for intuitive endoscopic visualization, the first step is to integrate the magnetic localization result ${}^g\mathrm{T}_{\mathbf{m}_i}$ into the EVs. Additionally, magnetic attraction force information, estimated based on ${}^g\mathrm{T}_{\mathbf{m}_i}$ and the magnetic force model, can also be rendered into the EVs as a reference for surgeons. Furthermore, warning indicators can be generated based on the magnetic localization and attraction force information, providing real-time guidance and alerts.

1) Magnetic Localization Information Guiding: As illustrated in Fig. 5(a), define the endoscopic camera coordinate system in the i-th Endo-MagCap as ${}^{\mathbf{cam}_i}\mathcal{O}$. With the feedback from surgeons, the field of view of most of the endoscopes is less than 180°. Hence, the pinhole camera model is utilized in this article. First, define $\mathbf{I}_i = \begin{bmatrix} u_i & v_i \end{bmatrix}^\top \in \mathbb{R}^2$ as the compression magnet pixel information for the endoscope with i-th Endo-MagCap.

IEEE Transactions on Robotics (T-RO) paper, presented at ICRA 2026, Vienna, Austria. Cite as T-RO paper.

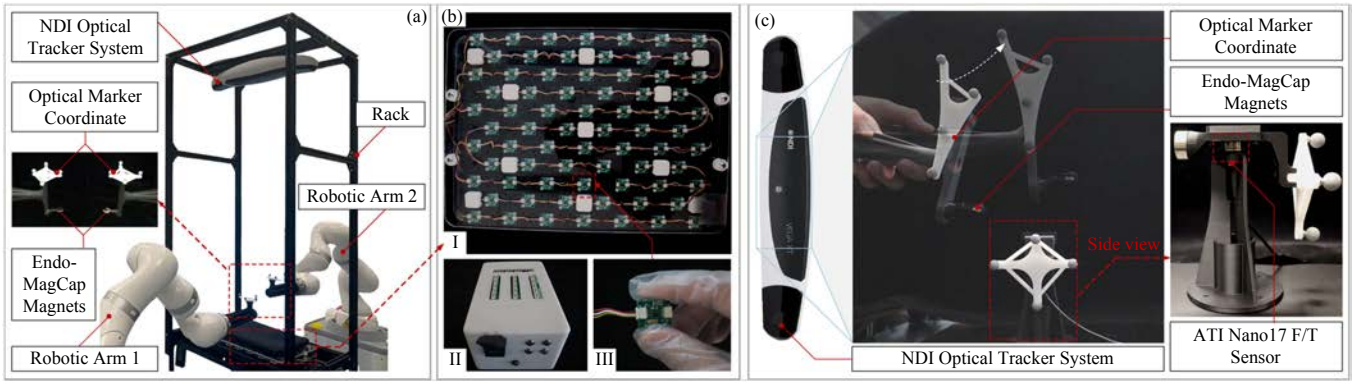

Fig. 6. Setups for the preliminary and multimagnetic six-DoF localization and magnetic attraction force experiments. (a) Multimagnetic six-DoF localization experimental setup. Two robotic arms hold Endo-MagCap and optical marker coordinates to move in the measurement space of both the lower magnetic localization system and the upper NDI optical tracker system. (b) Illustration of the magnetic localization system. I: Magnetic sensor pad; II: Self-developed magnetic field collection module based on STM32 MCU; III: Magnetic sensor based on Melexis MLX90393. (c) Setup for magnetic attraction force experiments. Endo-MagCap 1 is fixed on ATI Nano17 Titanium F/T sensor while Endo-MagCap 2 moves in the space around Endo-MagCap 1. Both Endo-MagCap are attached with optical marker coordinates, which move in the measurement space of the NDI optical tracker system in the side.

Then, the pinhole camera model in [41] is recalled as

$$s_i \begin{bmatrix} \mathbf{I}_i^\top & 1 \end{bmatrix}^\top = \mathbf{K}_i \begin{bmatrix} {}^{\mathbf{cam}_i}\mathbf{R}_{\mathbf{m}_j} & {}^{\mathbf{cam}_i}\mathbf{P}_{\mathbf{m}_j} \end{bmatrix} \begin{bmatrix} \mathbf{P}_{\mathbf{m}_j}^\top & 1 \end{bmatrix}^\top \tag{22}$$

where $s_i \in \mathbb{R}^+$ is the scale factor and ${}^{\mathbf{cam}_i}\mathbf{R}_{\mathbf{m}_j} \in \mathbb{SO}(3)$ and ${}^{\mathbf{cam}_i}\mathbf{P}_{\mathbf{m}_j} \in \mathbb{R}^3$ are the orientation matrix and translation ~~vector~~ in ${}^{\mathbf{cam}_i}\mathrm{T}_{\mathbf{m}_j} \in \mathbb{SE}(3)$, which can be inferred by

$$\begin{aligned} {}^{\mathbf{cam}_i}\mathrm{T}_{\mathbf{m}_j} &= \begin{bmatrix} {}^{\mathbf{cam}_i}\mathbf{R}_{\mathbf{mj}} & {}^{\mathbf{cam}_i}\mathbf{P}_{\mathbf{mj}} \\ \mathbb{O}_{1\times 3} & 1 \end{bmatrix} \\ &= \left({}^{\mathbf{m}_i}\mathrm{T}_{\mathbf{cam}_i}\right)^{-1} \left({}^{g}\mathrm{T}_{\mathbf{m}_i}\right)^{-1} {}^{g}\mathrm{T}_{\mathbf{m}_j} \end{aligned} \tag{23}$$

where the known transformation ${}^{\mathbf{m}_i}\mathrm{T}_{\mathbf{cam}_i} \in \mathbb{SE}(3)$ between ${}^{\mathbf{cam}_i}\mathcal{O}$ and ${}^{\mathbf{m}_i}\mathcal{O}$ shows that there is a rigid connection between the endoscope camera and the Endo-MagCap as indicated in Fig. 3. Noting that ${}^{\mathbf{cam}_i}\mathrm{T}_{\mathbf{m}_j}$ present the transformation relation from the frame coordinate of endoscopic camera ${}^{\mathbf{cam}_i}\mathcal{O}$ to the j compression magnet frame coordinate ${}^{\mathbf{m}_j}\mathcal{O}$, as shown in Fig. 5(a). Besides, $\mathbf{K}_i$ in (22) is the camera intrinsic matrix with the following definition:

$$\mathbf{K}_i = \begin{bmatrix} f_{x,i} & 0 & c_{x,i} \\ 0 & f_{y,i} & c_{y,i} \\ 0 & 0 & 1 \end{bmatrix} \in \mathbb{R}^{3\times 3}$$

where $\begin{pmatrix} f_{x,i} & f_{y,i} \end{pmatrix}$ and $\begin{pmatrix} c_{x,i} & c_{y,i} \end{pmatrix}$ are the focal lengths and the principal points, respectively, for the endoscopic camera with the i-th compression magnet. Based on the calculation of (23), the compression magnet pixel information $\mathbf{I}_i$ for the EVs can be obtained via (22), which is marked as an unit-length arrow guiding in EVs as shown in Fig. 5(c). Additionally, ${}^{\mathbf{cam}_i}\mathbf{P}_{\mathbf{m}_j}$ is also significant information, which is shown in axial component x, y, and z as indicated in Fig. 5(b).

Moreover, the other significant information, the estimated distance between these two compression magnets in Endo-MagCap, can be acquired by using the magnetic localization results, which can be defined as the following:

$$\mathrm{dist}\left(\mathbf{P}_{\mathbf{m}_1}, \mathbf{P}_{\mathbf{m}_2}\right) = \left\|\mathbf{P}_{\mathbf{m}_1} - \mathbf{P}_{\mathbf{m}_2}\right\|_2 \tag{24}$$

where $\mathrm{dist}(\mathbf{P}_{\mathbf{m}_1}, \mathbf{P}_{\mathbf{m}_2}) \in \mathbb{R}^+$ is the Euclidean distance between two compression magnets. This information can be indicated on EVs for surgeons, as illustrated in Fig. 5(b). Furthermore, the thickness of the unit-length arrow guiding in EVs is designed to vary based on $\mathrm{dist}(\mathbf{P}_{\mathbf{m}_1}, \mathbf{P}_{\mathbf{m}_2})$. When, $\mathrm{dist}(\mathbf{P}_{\mathbf{m}_1}, \mathbf{P}_{\mathbf{m}_2})$ increases, the thickness is larger for warning referencing, which can be seen in Figs. 5(b) and 11(a).

2) Estimated Magnetic Attraction Force Referencing: Assuming that the magnetic field of the compression magnet can be modeled using the dipole model (2), and that the magnetic wrench from the localization magnets can be neglected due to their customized placement at a greater distance from the compression magnet (compared to the minimal compression distance), the magnetic attraction force $\mathbf{F}(\mathbf{m}_{i,j}, \mathbf{P}_{\mathbf{m}_{ij}}) \in \mathbb{R}^3$ can be approximately expressed as

$$\begin{aligned} \mathbf{F}\left(\mathbf{m}_{i,j}, \mathbf{P}_{\mathbf{m}_{ij}}\right) \approx \frac{3\mu_0}{4\pi \left\|\mathbf{P}_{\mathbf{m}_{ij}}\right\|^4} \Bigg\{ &\left(\hat{\mathbf{P}}_{\mathbf{m}_{ij}}^\top \mathbf{m}_j\right)\mathbf{m}_i + \left(\hat{\mathbf{P}}_{\mathbf{m}_{ij}}^\top \times \mathbf{m}_i\right)\mathbf{m}_j \\ &+ \left[\mathbf{m}_i^\top \mathbf{m}_j - 5\left(\hat{\mathbf{P}}_{\mathbf{m}_{ij}}^\top \mathbf{m}_i\right)\left(\hat{\mathbf{P}}_{\mathbf{m}_{ij}}^\top \mathbf{m}_j\right)\right]\hat{\mathbf{P}}_{\mathbf{m}_{ij}} \Bigg\} \end{aligned} \tag{25}$$

with the following:

$$\mathbf{P}_{\mathbf{m}_{ij}} = \mathbf{P}_{\mathbf{m}_j} - \mathbf{P}_{\mathbf{m}_i}, \hat{\mathbf{P}}_{\mathbf{m}_{ij}} = \mathbf{P}_{\mathbf{m}_{ij}} / \left\|\mathbf{P}_{\mathbf{m}_{ij}}\right\|$$

where $\mathbf{P}_{\mathbf{m}_{ij}} \in \mathbb{R}^3$ is the relative location of the compression magnets. Based on (25), the estimated norm magnetic attraction force

$$\mathrm{force}\left(\mathbf{m}_{i,j}, \mathbf{P}_{\mathbf{m}_{ij}}\right) = \left\|\mathbf{F}\left(\mathbf{m}_{i,j}, \mathbf{P}_{\mathbf{m}_{ij}}\right)\right\|_2 \tag{26}$$

between two compression magnets can be obtained and rendered in EVs as referencing information as shown in Fig. 5(b).

3) Compression Warning Information: Based on the above Euclidean distance (24) and magnetic attraction force (25), the warning indication can be displayed on the EV when the following conditions are satisfied:

$$\mathrm{dist}\left(\mathbf{P}_{\mathbf{m}_1}, \mathbf{P}_{\mathbf{m}_2}\right) \leqslant \overline{\mathrm{dist}}, \text{ or } \mathrm{force}\left(\mathbf{m}_{i,j}, \mathbf{P}_{\mathbf{m}_{ij}}\right) \geq \underline{\mathrm{f}}$$

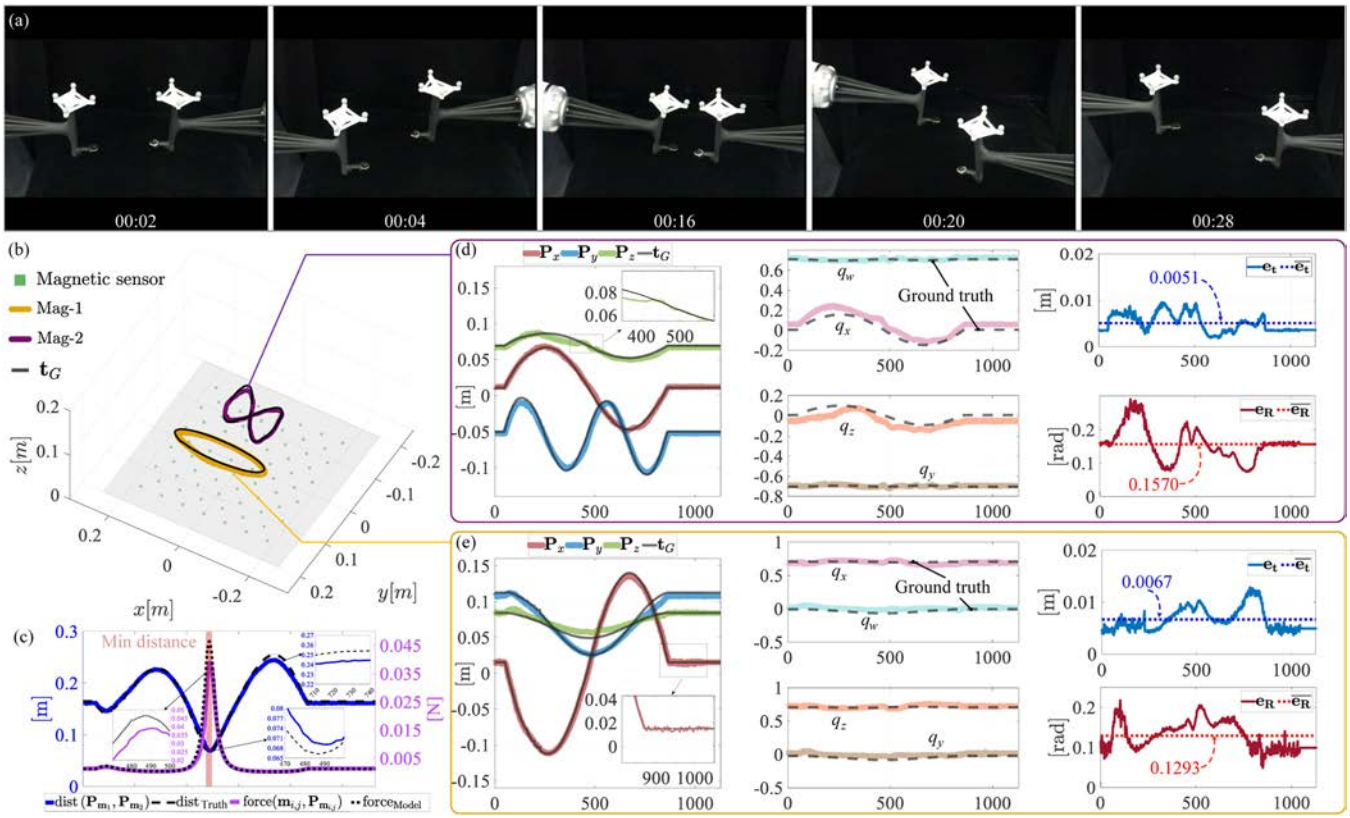

Fig. 7. Illustrations of multimagnetic six-DoF localization for two Endo-MagCaps (Mag-1 and Mag-2) and localization results. (a) Illustration of the movement process of two Endo-MagCaps by a robotic arm in different frames from 00:02 to 00:28. (b) 3-D ground-truth trajectory and localization trajectory illustration and relative legends. (c) Results of the estimated Euclidean distance and norm of magnetic attraction force between two Endo-MagCaps during the test based on (25). (d) Localization results for the Mag-2 in position $\mathbf{P}_{\mathbf{m}_2} = [\mathbf{P}_x\ \mathbf{P}_y\ \mathbf{P}_z]^\top$ and orientation $\mathbf{Q}_{\mathbf{m}_2} = [\mathbf{q}_w\ \mathbf{q}_x\ \mathbf{q}_y\ \mathbf{q}_z]^\top$ and ground-truth reference, and the respective error results. (e) Localization results for the Mag-1 in position $\mathbf{P}_{\mathbf{m}_1} = [\mathbf{P}_x\ \mathbf{P}_y\ \mathbf{P}_z]^\top$ and orientation $\mathbf{Q}_{\mathbf{m}_1} = [\mathbf{q}_w\ \mathbf{q}_x\ \mathbf{q}_y\ \mathbf{q}_z]^\top$ and ground-truth reference, and the respective error results. More details refer to Video 1 in the Supplementary Video.

TABLE I
LOCALIZATION ERRORS AND ESTIMATED DISTANCE AND FORCE

		$\overline{e_\mathbf{t}}$	$\overline{e_\mathbf{R}}$	Min dist case			
				$\text{dist}_{\text{Truth}}$	$\text{dist}_{\text{MagsL}}$	$\text{force}_{\text{Model}}$	$\text{force}_{\text{MagsL}}$
Test I-1	Mag-1	0.0067	0.1293	0.0662	0.0694	0.0464	0.0381
	Mag-2	0.0051	0.1570				
Test I-2	Mag-1	0.0073	0.1556	0.0656	0.0745	0.0485	0.0285
	Mag-2	0.0085	0.1832				
Test I-3	Mag-1	0.0069	0.1461	0.0663	0.0756	0.0459	0.0266
	Mag-2	0.0076	0.1760				
Average	**Mag-1**	**0.0070**	**0.1437**	**0.0660**	**0.0732**	**0.0469**	**0.0311**
	Mag-2	**0.0071**	**0.1721**				

where $\overline{\text{dist}}$ and $\underline{\text{f}} \in \mathbb{R}^+$ are the threshold distance and force, respectively. When one of these conditions is triggered, the warning indication can be presented as shown in Fig. 5(d). Here ends the HUD guiding scheme design for EVs in endoluminal MCA.

IV. EXPERIMENTS

This section details the experiments conducted to validate the feasibility of the multimagnetic six-DoF localization algorithm and to quantify its accuracy. Furthermore, the effectiveness of the proposed MagsL-HUD endoscopic system is demonstrated through porcine ex vivo experimental designs.

A. Preliminary Laboratory Experiment

This section introduces the laboratory experiment setup for quantitative tests and preliminary work for the endoscopic visualization.

1) Magnetic Localization and Force Tests' Setup: As shown in Fig. 6(a), the quantitative localization test is conducted by setting up the platform consisting of a magnetic localization system, an optical tracker system, and robotic arms. Precisely, on the bottom of the rack, the developed magnetic localization system consists of 72 three-axis magnetic sensors (Melexis MLX90393 in Fig. 6(b-III), arranged in a 7×6 grid with 60 mm spacing and an inner 6×5 grid with 60 mm spacing as indicated in Fig. 6(b-I) (two grids are cross mounted with 30 mm gaps). Besides, a magnetic field collection module is designed based on an STM32F103 MCU to collect magnetic field data of all 72 three-axis magnetic sensors via IIC communication, as indicated in Figs. 6(b-II) and 9(b). Moreover, on the top of the rack, an optical tracker system (NDI Polaris Vega XT, accuracy: 0.15 mm) is deployed to measure the optical marker coordinate, which is attached to the Endo-MagCap magnets with a confirmed transformation relation. These magnets are cylinders for compression magnet with $\phi 20 \times 4$ mm and ring for localization magnet with inner $\phi 16$ mm and outer $\phi 23$ mm and a thickness of 10 mm (NdFeB with N52 grade). Furthermore,

IEEE Transactions on Robotics (T-RO) paper, presented at ICRA 2026, Vienna, Austria. Cite as T-RO paper.

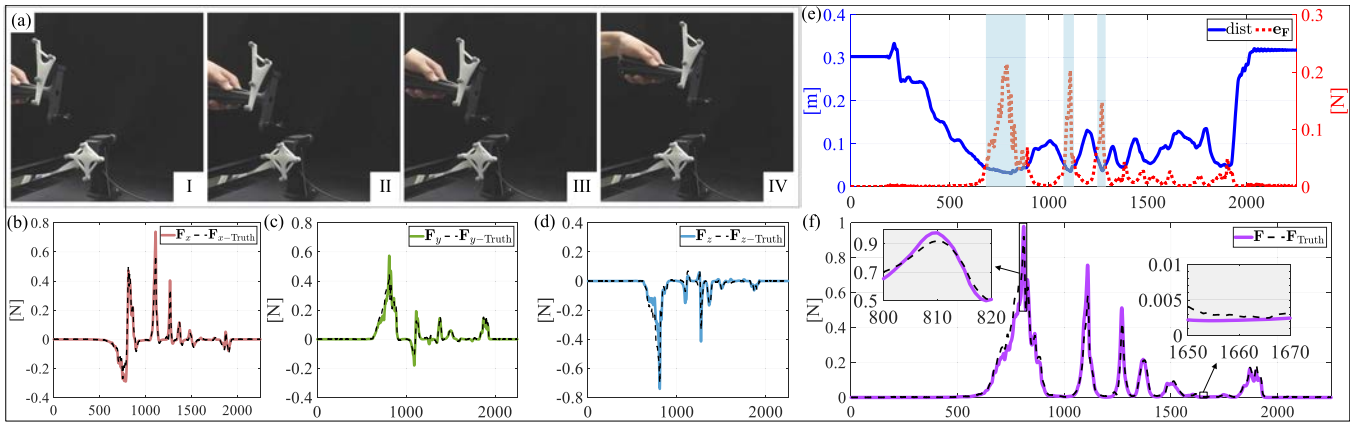

Fig. 8. Illustrations of the magnetic attraction force test and results. (a) Illustrations of the movement process of Endo-MagCap regarding the static Endo-MagCap fixed onto the force/torque sensor. (b) Measured ground-truth force and the results from (25) in x axis. (c) Measured ground-truth force and the results from (25) in y axis. (d) Measured ground-truth force and the results from (25) in z axis. (e) Results of the measured ground-truth Euclidean distance and force error $e_\mathbf{F}$ between the measured and that from (25). (f) Measured ground-truth norm force and the norm force results from (25). More details refer to Video 2 in the Supplementary Video.

aside from the rack, there are two robotic arms holding the optical marker coordinate and Endo-MagCap magnets to move in the desired trajectory, as indicated in Figs. 6(a) and 7(a).

Additionally, as illustrated in Fig. 6(c), the quantitative force test is performed on a setup consisting of a force/torque sensor (ATI Nano17 Titanium, sensing ranges 8 N in x, y axis and 14.1 N in z- axis with resolutions 1/682 N for x, y, z axes) and an optical tracker system as previously mentioned. Specifically, a 3-D-printed holder is designed to hold the force/torque sensor, on top of which is fixed a static Endo-MagCap 1 and an optical marker coordinate with a confirmed transformation. Besides, the Endo-MagCap 2 is mounted on a holder with an optical marker coordinate to move in different poses with respect to the static Endo-MagCap 1.

2) Evaluation Definitions: The optical tracking information for the i compression magnet is regarded as the ground-truth $\mathbf{G}_i(k) \in \mathbb{SE}(3)$ in sampling time $k \in \{1, 2, \ldots, T\}$, which is used to compare with the magnetic localization results obtained via the developed system and algorithm. Notably, the information $\mathbf{G}_i(k)$ obtained via the optical tracker system is respective to itself coordinate system. Therefore, the necessary calibration process should be performed to calculate the transformation ${}^g\mathrm{T}_{\text{optical}}$ between the optical tracker system and the global frame coordinate ${}^g\mathcal{O}$. Then the ground-truth with respect to ${}^g\mathcal{O}$ can be formed as

$$ {}^g\mathbf{G}_i(k) = {}^g\,\mathrm{T}_{\text{optical}}\mathbf{G}_i(k) = \begin{bmatrix} \mathbf{R}_G(k,i) & \mathbf{t}_G(k,i) \\ \mathbb{O}_{1\times 3} & 1 \end{bmatrix}. \quad (27) $$

Based on the measured $(\mathbf{P}_{\mathbf{m}_i,k}, \mathbf{Q}_{\mathbf{m}_i,k})$ and the results in (27), the mean position and orientation accuracy can be evaluated, respectively, by

$$ \overline{e_\mathbf{t}}(i) = \frac{1}{T}\sum_k e_\mathbf{t}(k,i), \overline{e_\mathbf{R}}(i) = \frac{1}{T}\sum_k e_\mathbf{R}(k,i) \quad (28) $$

with $e_\mathbf{t}(k,i) = \|\mathbf{t}_G(k,i) - \mathbf{P}_{\mathbf{m}_i,k}\|_2$ and $e_\mathbf{R}(k,i) = \|\mathrm{Log}(\mathbf{R}_G(k,i)\mathbf{R}^\top_{\mathbf{m}_i,k})\|_2$, where $\mathbf{R}_{\mathbf{m}_i,k}$ is calculated by transforming $\mathbf{Q}_{\mathbf{m}_i,k}$ via method in (12). Additionally, the measured force information is regarded as $\mathbf{F}_{\text{Truth}(k)} = [\mathrm{F}_{x-\text{Truth}}(k)\ \mathrm{F}_{y-\text{Truth}}(k)\ \mathrm{F}_{z-\text{Truth}}(k)]^\top \in \mathbb{R}^3$ and the norm and mean force error can be defined, respectively, as

$$ e_\mathbf{F}(k) = \|\mathbf{F}_{\text{Truth}}(k) - \mathbf{F}(\mathbf{m}_{i,j}, \mathbf{P}_{\mathbf{m}_{ij}})\|_2,\ \overline{e_\mathbf{F}} = \frac{1}{T}\sum_k e_\mathbf{F}(k). \quad (29) $$

3) Endoscopes' Camera Calibration: The implementation of HUD guiding information is based on model (22), which requires the camera intrinsic matrix $\mathbf{K}_i$. Based on the procedure and analysis in Appendix B, the parameters for $\mathbf{K}_i$ for endoscopic systems are obtained and listed in Table V, where $\mathbf{K}_1$ and $\mathbf{K}_2$ are the camera intrinsic matrices for the gastroscope and colonoscope, respectively, which further contribute to the ex vivo endoluminal MCA experiments.

B. Magnetic Localization Quantitative Experiment

In this section, the laboratory experiment is first carried out to quantitatively evaluate the accuracy of the developed localization system and algorithm.

Based on the experimental setup described in Section IV-A, quantitative magnetic localization experiments are conducted using robotic arm 1 and robotic arm 2 to move Endo-MagCap 1 and Endo-MagCap 2 along circular and "8" type trajectories, respectively, as illustrated in Fig. 7(a). Meanwhile, the developed magnetic field collection module records the magnetic field data and transmits it to the computer, where the proposed Algorithm 1 is executed. Simultaneously, the optical tracking system captures the ground-truth positions and orientations of Endo-MagCap 1 and 2 for validation.

The experimental results are illustrated in Fig. 7(b) and (d)–(e), which indicate the detailed position data $\mathbf{P}_{\mathbf{m}_i}(k)$ and orientation data $\mathbf{Q}_{\mathbf{m}_i}(k)$ in quaternion in sampling time as well as corresponding ground-truth data ${}^g\mathbf{G}_i(k)$. Moreover, the errors in position $e_\mathbf{t}$ and orientation $e_\mathbf{R}$ are calculated based on (28) and the results are showcased in Fig. 7(d) and (e). For such two Endo-MagCaps localization cases, as listed in

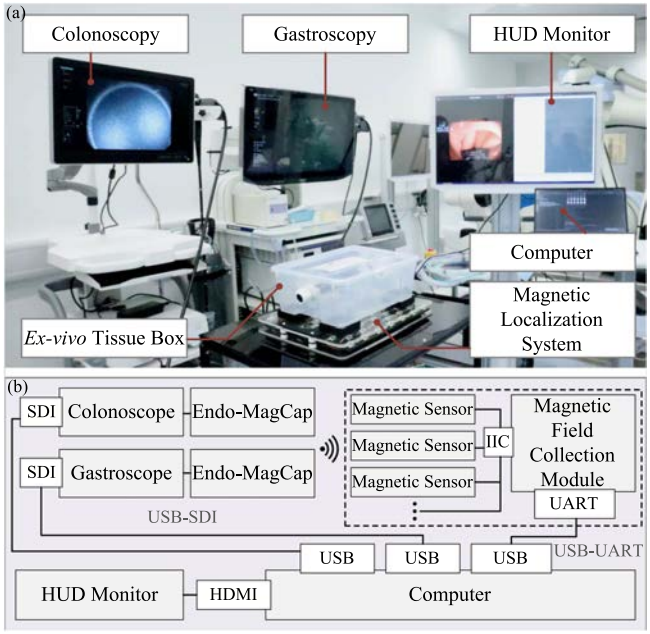

Fig. 9. Setup for the porcine ex vivo trials and overall hardware architecture. (a) MagsL-HUD endoscopic system illustration in a hybrid surgery operation room for the porcine ex vivo trial to conduct endoluminal MCA surgery. (b) Overall hardware architecture illustration for the MagsL-HUD endoscopic system regarding the setup in hybrid surgery operation room.

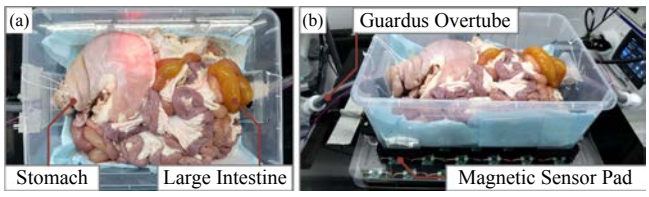

Fig. 10. Setup for the porcine ex vivo tissue preparation. (a) Illustration of the porcine ex vivo digestive system in ex vivo tissue box, in which the stomach, the large intestine and other tissues can be seen. (b) Illustration of the ex vivo tissue box setup onto the magnetic sensor pad and the utilization of Guardus Overtube on two sides.

Table I, results indicate that the average mean position and orientation accuracy in Endo-MagCap Mag-1 are $\overline{e_{\mathbf{t}}}(1)$ =0.0070 m and $\overline{e_{\mathbf{R}}}(1)$ =0.1437 rad, respectively, for circular trajectory, and that of Endo-MagCap Mag-2 are $\overline{e_{\mathbf{t}}}(2)$ =0.0071 m and $\overline{e_{\mathbf{R}}}(2)$ =0.1721 rad, respectively, for "8" type trajectory.

In addition, the estimated Euclidean distance and magnetic attraction force between the two Endo-MagCap (using ${}^{\mathbf{m}_i}\mathcal{O}$ as the coordinate frame for Endo-MagCap, since the position of compression magnets is critical in endoluminal MCA surgery) are calculated via (24) and (25), respectively. As illustrated in Fig. 7(b), the results demonstrate that the proposed estimated Euclidean distance closely aligns with the ground-truth Euclidean distance, represented by the black-dashed line in Fig. 7(c), which is obtained by substituting $\mathbf{t}_G(k,1)$ and $\mathbf{t}_G(k,2)$ into (24).

Notably, as indicated in Table I, in the minimal dist case in Test I-2, the estimated Euclidean distance $\text{dist}_{\text{MagsL}} = 0.0745$ m, compared to the ground-truth value of $\text{dist}_{\text{Truth}} = 0.0656$ m, resulting in an error $e_{\mathbf{t}}$ of 0.0089 m. Similarly, the estimated magnetic attraction force (black-dotted line) $\text{force}_{\text{Model}}$ via (25) based on the ground-truth distance data, and that based on magnetic localization Euclidean distance is shown in Fig. 7(c). At the minimal distance in Test I-2, the estimated magnetic attraction force is 0.0285 N, while the magnetic attraction force value based on ground-truth distance is 0.0485 N, resulting in a force error of 0.0200 N. These results indicate that the proposed localization system and multimagnetic six-DoF localization method can achieve reliable six-DoF tracking for two Endo-MagCaps, even in close-proximity scenarios.

TABLE II
FORCE TESTS ERRORS AND AVERAGE VALUE

	Test II-1	Test II-2	Test II-3	Test II-4	Test II-5	**Average**
$\overline{e_{\mathbf{F}}}$	0.0412	0.0215	0.0254	0.0581	0.0197	**0.0332**

C. Estimated Magnetic Attraction Force Experiment

In this section, the laboratory experiment is performed to test the magnetic attraction force accuracy of model (25).

The experimental setup is described in Section IV-A. The movable Endo-MagCap moves in different positions and orientations while the force/torque sensor and optical tracker system record the ground-truth force $\mathbf{F}_{\text{Truth}}$ and poses data $\mathbf{G}_i$, respectively. Then, using $\mathbf{G}_i$, the transformation between static Endo-MagCap and movable Endo-MagCap can be obtained by

$$^{\text{static}}\mathbf{T}_{\text{mov}} = \mathbf{G}_1^{-1}\mathbf{G}_2 = \begin{bmatrix} \mathbf{R}_{\text{mov}} & \mathbf{t}_{\text{mov}} \\ \mathbb{O}_{1\times 3} & 1 \end{bmatrix} \in \mathbb{SE}(3).$$

Let $\mathbf{m}_i = \|\mathbf{m}_i\|\,\hat{x}, \mathbf{m}_j = \|\mathbf{m}_j\|\,\mathbf{R}_{\text{mov}}\,\hat{x}$ and $\mathbf{P}_{\mathbf{m}_{ij}} = \mathbf{t}_{\text{mov}}$ in (25). Finally, the real-time measured $\mathbf{F}_{\text{Truth}}$ and the calculated $\mathbf{F}(\mathbf{m}_{i,j}, \mathbf{P}_{\mathbf{m}_{ij}})$ are illustrated in Fig. 8(b)–(d) in each axis, and the norm force results are indicated in Fig. 8(f). Based on (29), the mean force error $\overline{e_{\mathbf{F}}}$ is 0.0412 N in Test II-1. Besides, more tests are conducted and the mean force errors are listed in Table II for reference, which indicates an average mean force error of 0.0332 N.

Moreover, the results of the measured ground-truth Euclidean distance and force error $e_{\mathbf{F}}$ between the measured and that of (25) are illustrated in Fig. 8(e). It is found that the force error increases while these two Endo-MagCaps move closer (highlighted in light-cyan regions) since the assumption in the magnetic dipole model [36]. In all, it is concluded that (25) is a solution for the compression warning force reference for the designed Endo-MagCap, with an average mean error of 0.0332 N based on these tests.

D. Endoluminal MCA Surgery Verification in Ex Vivo Trials

In this section, trials are conducted using porcine ex vivo digestive systems to demonstrate the feasibility and advantages of the MagsL-HUD endoscopic system for endoluminal MCA surgery.

1) Ex Vivo Experimental Setup in Hybrid Surgery Operation Room: As shown in Fig. 9(a), the experimental setup comprises

IEEE Transactions on Robotics (T-RO) paper, presented at ICRA 2026, Vienna, Austria. Cite as T-RO paper.

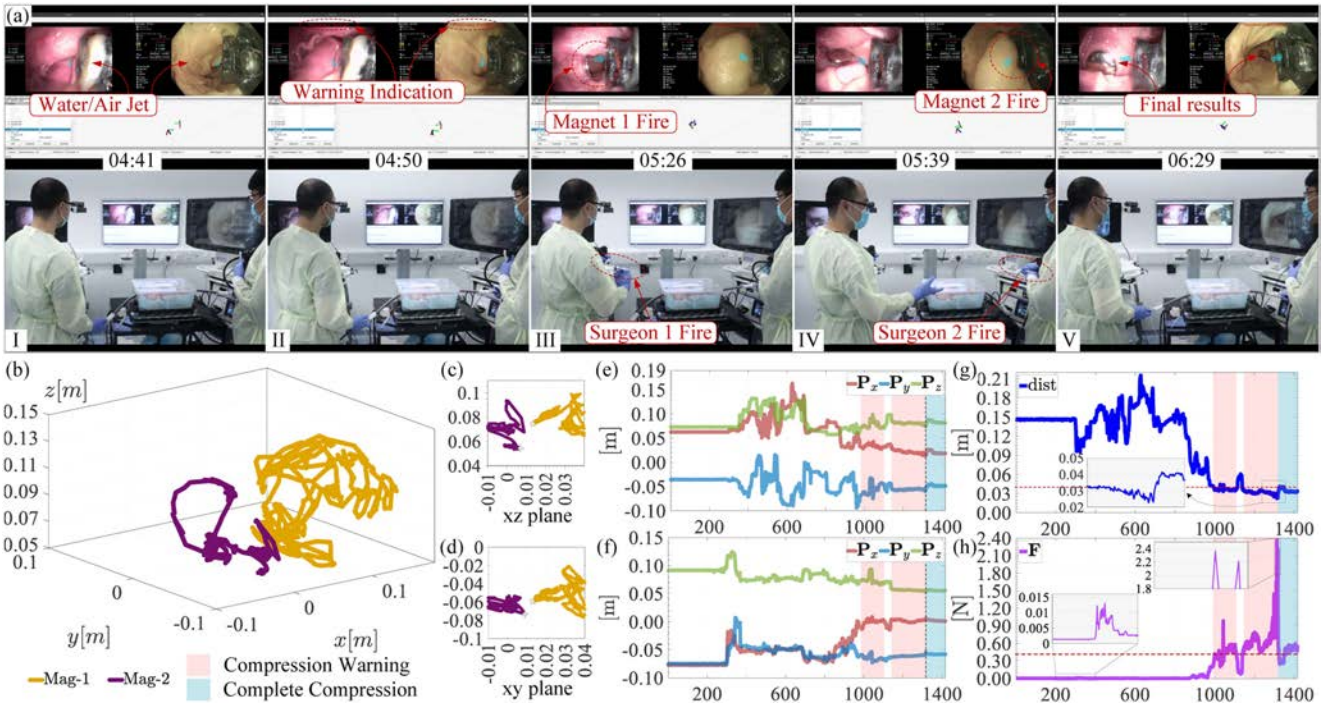

Fig. 11. Illustrations of performing porcine ex vivo MCA surgery using the MagsL-HUD endoscopic system and the results. (a) Illustrations of conducting porcine ex vivo MCA surgery in different steps and the intuitive HUD display. (b) 3-D movement trajectory for two compression magnets in Endo-MagCap. (c) Projections of 3-D movement trajectory for two compression magnets in xz plane. (d) Projections of 3-D movement trajectory for two compression magnets in xy plane. (e) Displacements in x-, y-, and z-axes of compression magnet 1 (Mag-1). (f) Displacements in x, y and z axis of compression magnet 2 (Mag-2). (g) Estimated Euclidean distance between these two compression magnets in Endo-MagCap. (h) Estimated norm of magnetic attraction force between these two compression magnets in Endo-MagCap. More details, refer to Video 3 in the Supplementary Video.

TABLE III
KEY PARAMETER IN ENDOLUMINAL MCA

	dist	force
In switch moment	0.02265 m	2.3666 N
Final static case⋆	≈ 0.00726 m	CF = 25.1072 N ≈ 25 N (FEM)

⋆: Results from X-Ray imaging using 3D Slicer.

one colonoscope (HD-350, SonoScape Medical) and one gastroscope (GIF-EZ1500, Olympus) which are equipped with Endo-MagCap as illustrated in Fig. 3(f). Besides, there is an LCD monitor (OEV321UH 4K Ultra High-Definition, Olympus) which is treated as an HUD monitor for intuitive interface screenings. Moreover, an ex vivo tissue box (0.3 m in width, 0.42 m in length, 0.25 m in height) holds the porcine ex vivo tissue which is mounted above the developed localization system as indicated in Figs. 9(a) and 10(b). More details about the porcine ex vivo digestive system are shown in Fig. 10, in which the stomach and intestines are set up in as real positions as possible. For subsequent surgery operations, orifices in the stomach and large intestine are connected to Guardus Overtube (STERIS) for better endoscope insertion, as indicated in Fig. 10(b).

Moreover, the overall hardware and communication architecture is illustrated in Fig. 9(b). The proposed multimagnetic localization six-DoF algorithm and HUD synchronization are executed on a computer (implemented in C++ and demonstrated in MATLAB, running on a 2.90 GHz Core i7-10700 CPU with an Ubuntu 20.04 operating system). Specifically, the computer receives magnetic field data ${}^{g}\mathbf{B}$ via the magnetic field collection module using USB-UART communication and captures endoscopic images through USB-SDI communication via the SDI capture card. Finally, the computer transmits the intuitive EVs to the HUD monitor via HDMI output.

2) Porcine Ex Vivo Trials: As illustrated in Fig. 11(a), two surgeons are performing endoluminal MCA surgery on a porcine ex vivo digestive system using the proposed MagsL-HUD endoscopic system. The experimental procedure is primarily conducted as follows.

Step 1: Surgeons insert the endoscopes equipped with the Endo-MagCap through the Guardus Overtube. The endoscopes are advanced into the unstructured endoluminal environment, as illustrated in Fig. 11(a-I). During this process, surgeons can use water or air jets to clean the endoscope and inflate the duct as needed.

Step 2: The MagsL-HUD endoscopic system is activated, providing real-time magnetic localization information and guiding references on the HUD monitor. Guided by the HUD display, surgeons maneuver the endoscopes to advance and align the compression magnets for closer proximity.

Step 3: Based on the surgeons' manoeuvres, compression warning indicators appear on top of the intuitive endoscopic images, as shown in Fig. 11(a-II). Additionally, the real-time Euclidean distance and magnetic attraction force between the two compression magnets are displayed as references.

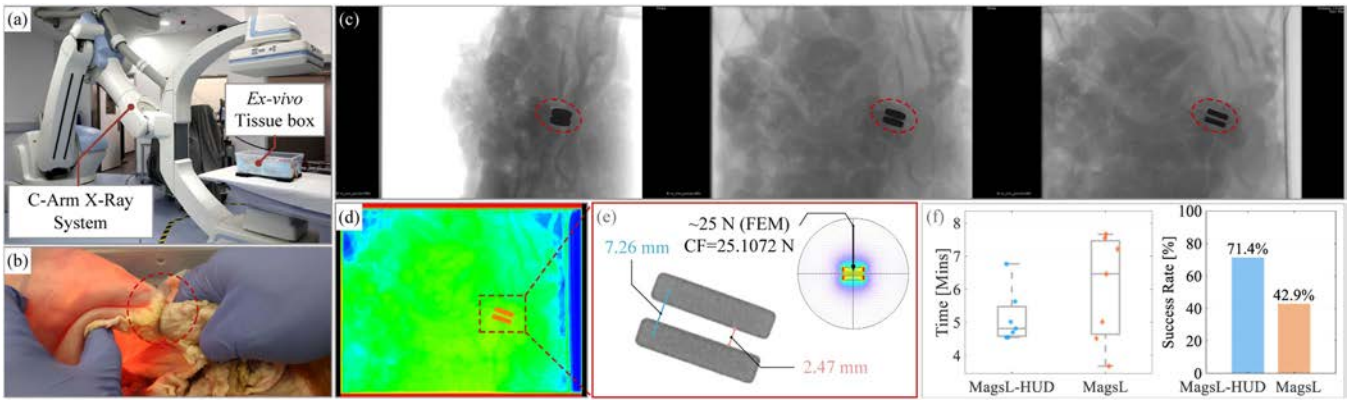

Fig. 12. Setup for 3-D X-ray image scanning and results using 3-D Slicer, as well as repeated comparative trial results. (a) Illustration of using C-Arm X-ray system to scan the porcine ex vivo tissue box after the endoluminal MCA surgery. (b) Surgeons perform an external inspection of the compression area after the endoluminal MCA surgery and 3-D X-ray image scanning. (c) Detailed view of the final complete compression results inside the porcine ex vivo tissue from three different perspectives (More details refer to the Video 4 in the Supplementary Video). (d) Illustration of a color-segmentation image, in which the compression magnets can be recognized. (e) Measurement results of geometric distance and gap distance between two compression magnets inside the porcine ex vivo tissue using the Measurement Tool in 3-D Slicer and compression force results based on FEM and a fitted polynomial model based on tests. (f) Results of operative time and success compression rate in repeated comparative trials of the MagsL-HUD versus only the MagsL methods.

Step 4: When the Euclidean distance between the compression magnets is reduced to approximately 0.035 m or less, surgeons use the pulling shaft to deploy the compression magnets.

Step 5: After deployment, surgeons retract the endoscopes to examine the compression results at each site of the duct, as illustrated in Fig. 11(a-V). Once the magnetic compression is confirmed, the endoscopes are fully withdrawn, completing the endoluminal MCA surgery on the porcine ex vivo digestive system.

Based on the above steps, it can be observed that at the moment 04:50, as shown in Fig. 11(a-II), the compression warning information is exhibited. Then, by controlling the endoscopes, surgeons guide the compression magnets closer together as the estimated Euclidean distance decreases, which is indicated in Fig. 11(g). When the distance is $\leqslant$ 0.035m, the up cover of Endo-MagCap is opened by surgeons as shown in Fig. 11(a-III) and (a-IV). The 3-D movement trajectory and displacements in the axis of compression magnets are illustrated in Fig. 11(b) and (e)–(f), respectively. For a better understanding, the Euclidean distance and magnetic attraction force between these two compression are indicated in Fig. 11(g) and (h), and the projections of 3-D movement trajectory in xz and xy planes are shown in Fig. 11(c) and (d), respectively. From these two planes, it can be found that two compression magnets move to get close at the end of the trajectory under surgeons' operations.

Besides, more clearly in Fig. 11(g) and (h), the Euclidean distance declines with fluctuation under the surgeons' handling with HUD information guiding. Through the comparison of time nodes, it has been divided into the last two states: compression warning and complete compression states, as illustrated in light-pink and light-cyan regions. It can be found that at the compression moment, the switch moment between two states, the Euclidean distance is 0.02265 m, and the magnetic attraction force is 2.3666 N.

In order to verify the successful magnetic compression result, a C-Arm X-ray system (Siemens Artis Zeego C-Arm X-ray, SIEMENS, Germany) is utilized to capture 3-D X-ray images of the porcine ex vivo tissue inside the box, as illustrated in Fig. 12(a). Moreover, by processing 3-D X-ray images in 3-D Slicer software [42], the magnetic compression result can be clearly observed, as shown in Fig. 12(c), in which it offers a detailed view of the final complete compression results inside the porcine ex vivo tissue from three different perspectives. In order to have a clear visualization of the final compression result, the color-segmentation and bone images are indicated in Fig. 12(d) and (e). From these two figures, the compression magnets can be clearly recognized as being in a successful compression state. Moreover, by using the Measurement Tool in 3-D Slicer as indicated in Fig. 12(e), the final Euclidean distance between these two compression magnets is 0.00726 m approximately, and the gap between these two compression magnets is about 0.00247 m. As shown in Fig 12(e), based on these data, the final compression force is 25 N approximately by using FEM simulations and 25.1072 N from a fitted model based on tests in Section IV-E. All key parameters can be found in Table III. Furthermore, an external inspection of the compression area after the endoluminal MCA surgery and 3-D X-ray image scanning confirms a successful stomach-colon MCA, as shown in Fig. 12(b). These results demonstrate that this finally achieves a successful stomach-colon MCA case in unstructured digestive tracts using the MagsL-HUD endoscopic system. Furthermore, repeated comparative trials are conducted in a similar model setup. Seven trials are performed using the MagsL-HUD method, and seven control trials employed MagsL feedback alone. Quantitative analysis revealed that MagsL-HUD achieved shorter mean operative time (5.15 min versus 6.02 min) and higher compression success rate (71.4% versus 42.9%) compared to the MagsL method, as shown in Fig. 12(f). Observations identify distinct failure modes. MagsL-HUD failures (2 cases) resulted from: 1) endoscope tip movement during the final fire process as the surgeon put down the endoscope, and 2) inadequate workspace from insufficient tissue insufflation. MagsL failures (4 cases) stem from: 1) premature device release in three

IEEE Transactions on Robotics (T-RO) paper, presented at ICRA 2026, Vienna, Austria. Cite as T-RO paper.

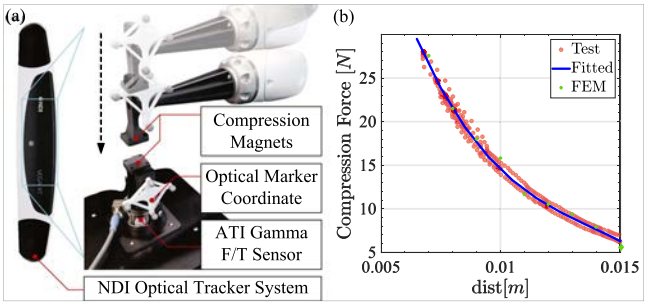

Fig. 13. Setup for compression force tests and results. (a) Setup for compression force experiments with side-to-side magnets. One compression magnet is fixed on the ATI Gamma F/T sensor, while the other compression magnet is held and moved by a robotic arm in a side-to-side pose. (b) Measured ground-truth compression force data, its fitted curve, and the results from the FEM simulation method.

cases, and 2) in one proximity case, magnetic interference during asynchronous firing led to one Endo-MagCap not being able to fire. In all, compared to the advantage in operative time, the improvement in success rate demonstrates the clinical value of the proposed MagsL-HUD endoscopic system. By providing feedback on compression warnings and magnetic attraction forces, the system enables surgeons to fire compression magnets within the proper distance, effectively preventing failures caused by inappropriate distance.

E. Compression Force Test on Side-to-Side Magnets

In this subsection, the compression force between side-to-side magnets is tested. As shown in Fig. 13(a), a robotic arm is used to hold one compression magnet to move close to the other compression magnet, which is fixed onto a force/torque sensor (ATI Gamma, sensing range 100 N in z-axis with resolution 1/80 N for z-axis). Both compression magnets are attached with optical marker coordinates, allowing the gap distance to be measured by an optical tracker system.

As shown in Fig. 13(b), results show that compression force increases as gap distance decreases with a fitted polynomial model as

$$CF = p_1 \times \text{dist}^3 + p_2 \times \text{dist}^2 + p_3 \times \text{dist} + p_4$$

($p_1 = -3.037 \times 10^7, p_2 = 1.267 \times 10^6, p_3 = -1.889 \times 10^4$, $p_4 = 107.1$ based on measured data), where CF is compression force in N unit. Besides, the FEM simulation results are marked in Fig. 13(b). It is observed that within a gap distance of 0.015 m, the FEM simulation results are closer to the actual measured results, compared to the dipole model in (25), which overestimates the force by one to two orders of magnitude. For magnetic analysis of this type of side-to-side magnets, refer to the results of FEM simulation to explore compression magnet design or control gap distance for the optimal compression force range [43].

F. Video Demonstration

To further enhance the visualization of experimental results, we have provided detailed video demonstrations for key experiments discussed in the article. These videos offer an in-depth, step-by-step visualization of both the experimental setup and the application of the MagsL-HUD system, ensuring a clearer understanding of its effectiveness in different contexts.

The first video showcases the localization experiment described in Section IV-B. The second video shows the measured ground-truth force and the results from (25) described in Section IV-C. The third video demonstrates the ex vivo MCA surgery performed using the proposed MagsL-HUD endoscopic system, as shown in Section IV-D. This video effectively highlights the real-world application of the system in a simulated clinical environment. The fourth video displays 3-D X-ray imaging results of the porcine ex vivo tissue, described in Section IV-D. This video offers a detailed view of various perspectives of the final complete compression results inside the porcine ex vivo tissue. The compression magnets can be seen, providing a comprehensive understanding of their final positioning.

V. Discussion

This study introduces the MagsL-HUD endoscopic system, an innovative solution that enhances endoluminal MCA surgery by providing real-time localization and intuitive endoscopic visualization. The integration of multimagnetic six-DoF localization with HUD guidance offers a promising approach to address the critical challenge of safe, real-time feedback in complex, unstructured endoluminal environments. This represents a significant step forward in improving the safety and efficacy of endoluminal MCA procedures. Additionally, the authors recognize the importance of considering and discussing the following relevant issues to offer deeper insights for readers and future researchers.

A. Consideration on Biocompatible Needs

The design and fabrication of the Endo-MagCap utilized 3-D printing technologies to achieve precise geometries and functional components. Given its application in surgical environments, careful consideration should be given to the choice of biocompatible materials. Materials such as polyetheretherketone (PEEK) and medical-grade polylactic acid are commonly used due to proven compatibility with human tissues and resistance to sterilization processes.

The magnets within the Endo-MagCap required specialized coatings to address two critical concerns: biocompatibility and corrosion resistance. Bare magnets, particularly those made of NdFeB, are prone to corrosion in physiological environments. To mitigate this, a multilayer coating approach should be adopted. 1) Base layer: A nickel-copper-nickel coating can be applied to improve corrosion resistance and mechanical durability. 2) Biocompatible outer layer: A final layer of medical-grade perylene can be added to ensure safety and biocompatibility. The coating process is optimized to maintain the magnetic strength of the magnets while preventing the leaching of potentially harmful substances into surrounding tissues.

B. Consideration on Instruments Interference

The instrument interference is an issue to be considered, as surgeons may utilize the endoscopic instrument channel during

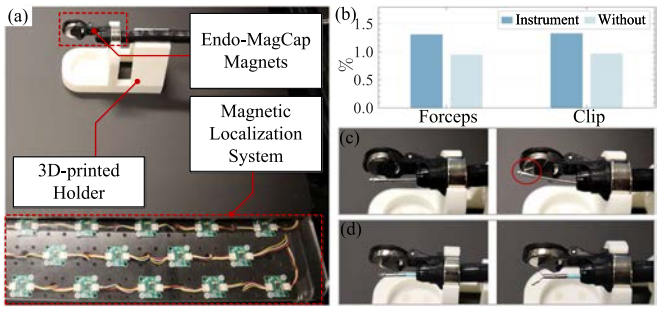

Fig. 14. Setup for instruments interference tests and results. (a) Setup for instruments' interference tests. One Endo-MagCap is fixed to the localization system, while the instruments can be inserted through the working channel to the tip. (b) Field percentage change results for the forceps and clip. (c) Interference observation for forceps. (d) Interference observation for the clip.

procedures. As shown in Fig. 14(a), the Endo-MagCap remains stationary while recording baseline magnetic field measurements ${}^{g}\mathbf{M}_{ori}(m,n)$ for each (m,n) magnetic sensor. Then, the variance in the magnetic field is measured as $\triangle^{g}\ \mathbf{M}(m,n)$ when instrument is introduced, and the attraction interference between the magnets and instrument is observed. The field percentage change is defined as

$$\rho = \frac{\sum^{m,n} \| \triangle^{g}\ \mathbf{M}(m,n)\|}{\sum^{m,n} \|{}^{g}\mathbf{M}_{ori}(m,n)\|} \times 100\%.$$

Fig. 14(b) shows test results for two common instruments: biopsy forceps and clips (both austenitic stainless steel), yielding ρ are 1.31% and 1.33%, respectively, (ρ for no-instrument cases are 0.95% and 0.97%, respectively). Besides, attractive magnetic interaction is observed with forceps as indicated in Fig. 14(c), and clips showed smaller interference as illustrated in Fig. 14(d). Consequently, we recommend avoiding stainless steel instruments when using the MagsL-HUD system in MCA surgery. When additional instruments are required, nonferromagnetic alternatives (e.g., medical-grade plastics or titanium) should be selected.

Furthermore, electrosurgical units pose additional electromagnetic compatibility concerns. When activated, these devices generate high-frequency electromagnetic fields that may couple with magnetic sensors. Such time-varying interference could corrupt measurements of the static magnetic fields, which are essential for localization accuracy. We recommend avoiding the use of electrosurgical units when using the MagsL-HUD system during MCA surgery.

C. Clinical Feedback and Enlightenment

Feedback from consulting surgeons provided valuable insights into the clinical utility and potential development of the proposed system. The key points are summarized as follows.

1) Surgeons appreciate the integration of localization data directly into the EV. Traditionally, compression magnet localization relies on X-ray imaging, which exposes both patients and surgeons to radiation and requires protective equipment. Furthermore, reconstructing spatial pose from 2-D X-ray images is challenging and unintuitive. While switching between imaging modalities is feasible, the HUD endoscope concept offers an intuitive and valuable solution for intraoperative guidance.
2) The technical framework and the initial validation results are promising. The core innovation lies in the combination of magnetic localization with endoscopic visualization. This technology could be extended to scenarios involving both endoscopes and capsules [25], [44], where a capsule carrying a magnet is positioned at a target site, and then an endoscope with Endo-MagCap is used for guided operation. This could broaden the clinical applicability of the system, particularly as the simultaneous operation of two endoscopes presents considerable skill challenges.
3) Endoluminal MCA has been shown to be feasible for anastomosis. However, from a clinical perspective, in cases such as intestinal obstruction, the new anastomosis may not form until at least two weeks postsurgery [13], which may not be ideal. Investigating the mechanisms of anastomosis formation after MCA, or exploring ways to accelerate tissue necrosis and healing, could be directions for future research.
4) For intestinal anastomosis, maintaining a patent lumen is critical. It was recommended that the anastomosis should have a big enough diameter to mitigate the risk of postoperative stricture. This suggests that the use of magnets with insufficient dimensions could potentially compromise the long-term success of the anastomosis, highlighting a key parameter for device design and selection.

D. Comparisons With Studies, Limitations, and Future Works

In recent clinical case studies, surgeons often face a tradeoff between NSW and RF procedures, as existing methods struggle to achieve both simultaneously. As indicated in Table IV, for example, techniques in [13] and [45] rely on open surgery or laparoscopic approaches, which are RF but compromise on NSW, resulting in tissue injury and prolonged recovery. In contrast, methods like [46] and [47] achieve NSW using X-ray imaging for feedback, yet expose patients and surgeons to harmful radiation. Our system uniquely integrates both NSW and RF capabilities, providing a safer and less invasive alternative. Unlike prior techniques that depend on open-vision or X-ray imaging, requiring surgeon interpretation, our approach directly delivers localization and force information, offering more intuitive feedback. Additionally, the HUD endoscope design aligns with surgeons' operational habits, enhancing procedural usability. However, our method has limitations. It requires a nonmagnetic interface environment as discussed in Section V-B, potentially necessitating additional techniques to mitigate interference, and demands accurate model verification for reliability. Currently validated on ex vivo porcine models, the ultimate goal is to transition to in vivo and human trials. While these ex vivo experiments provide critical preliminary data, further validation in live animal models and human subjects is essential to establish clinical reliability and support regulatory approval for broader adoption. Moreover, there are several areas for improvement and further research that will be essential for its clinical translation. The following points outline key directions for future work.

TABLE IV
COMPARISON WITH PREVIOUS STUDIES

Studies	NSW	RF	Feedbacks	Guiding	Delivery method	Study	Limitations
Ref [13], 2017	✗	✓	Open-vision	✗(-)	Surgeon intervention	Human	Tissue injury, longer hospital stays and slow-paced recovery
Ref [46], 2020	✓	✗	X-ray imaging	✗(-)	Endoscopy + Lithotripsy basket catheter	Human	Requires well-trained team and exposure on harmful radiation
Ref [45], 2023	✗	✓	Open-vision	✗(-)	Endoscopy + Special laparoscopic device	Porcine	Tissue injury in laparoscopic surgery
Ref [47], 2025	✓	✗	X-ray imaging	✗(-)	Endoscopy + Guidewire	Human	Requires expert-level skills and exposure on harmful radiation
This work	✓	✓	**Localization and force information**	✓**(HUD)**	**Endoscopy + Endo-MagCap**	***Ex vivo* porcine**	**Requires non-magnetic interference and accurate model verification**

1) Transitioning from ex vivo to in vivo testing, and further human trials: A critical next step is transitioning the system from ex vivo animal models to in vivo testing, and ultimately, human trials. The performance of the system must be evaluated under realistic surgical conditions to assess its feasibility in live human tissues. The next goal is to refine the system's ability to perform in real-world clinical environments.
2) Exploring 3-D sensor array localization system: The current 2-D magnetic sensor array used in the system limits the potential localization space. To overcome this constraint, exploring alternative sensor array configurations, such as 3-D sensor arrays [48], could provide more comprehensive spatial coverage. Further research into this 3-D sensor array approach can offer significant improvements in magnetic localization system measurement space.
3) Improvements in the HUD interface: The effectiveness of the HUD interface plays a significant role in guiding surgeons through the MCA procedure. Future work will involve refining the UI design of the HUD to enhance user experience and interaction. By making the interface more intuitive and responsive, surgeons will be able to make better-informed decisions in real-time.
4) Integration of magnetic actuation for automated performance: Future research can explore the introduction of external magnetic actuation sources, such as permanent magnets [49], [50] or electromagnets [38], [51], to enable closed-loop magnetic control and path planning under magnetic actuation [52], [53]. By integrating these actuation sources with EV-based imaging information, the system can achieve fully robotic magnetic manipulation during MCA surgery. The core challenge lies in the simultaneous localization and control of multiple magnetic devices, which, if successfully implemented, would significantly enhance the level of automation in MCA procedures.
5) Considerations for postoperative surgery: The MagsL-HUD system is validated for intraoperative navigation, with separate considerations necessary for postoperative monitoring. The positioning error of $\approx$0.007 m is acceptable during the challenging long-range guidance phase (navigating from $>$0.20 to $<$0.05 m), as it remains an order of magnitude smaller than the distances traversed and does not impede reliably reaching the magnetic capture zone. In contrast, at proximity ($<$0.05 m), magnetic self-alignment dominates, reducing reliance on precise guidance. Regarding force estimation, it achieves an average error of 0.0332 N during long-range navigation, providing helpful feedback. Although the error increases to $\approx$0.3 N at close range, this is clinically acceptable because the system no longer guides motion at that stage. For postoperative monitoring of tissue compression forces and necrosis, where submillimetre localization accuracy would be required, we acknowledge that our method is insufficient.

The future of this technology lies in fine-tuning these aspects to create a robust, biocompatible, and user-friendly system that can be applied to real-world clinical settings.

VI. CONCLUSION

In this article, we have introduced the MagsL-HUD endoscopic system, an innovative NSW/RF-compatible solution designed to enhance MCA surgeries, particularly in complex and unstructured endoluminal environments. By combining key technologies, such as the Endo-MagCap delivery device design, multimagnetic six-DoF localization, and real-time HUD guidance visualization, the MagsL-HUD system addressed critical limitations in current MCA procedures, specifically the lack of real-time RF localization feedback for compression magnets and provided effective visualization guidance for surgeons. Our experimental results, validated through laboratory experiments and ex vivo animal trials, demonstrated reliable tracking accuracy in both position and orientation. The system achieved six-DoF localization accuracy, with average errors of 0.0070 m and 0.1437 rad for one compression magnet in circular trajectory case, and 0.0071 m and 0.1721 rad for the other in "8" type trajectory case. Furthermore, porcine ex vivo trials confirmed the system feasibility and clinical applicability, successfully performing a stomach-colon MCA surgery with a final compression gap of approximately 0.00247 m. Comparative trials showed that the MagsL-HUD approach achieved a higher compression success rate than MagsL approach (71.4% versus 42.9%) in the designed trials. This improvement is attributed to real-time visualization of critical parameters, including distance, force, and warnings, which enhanced surgeons' ability to deploy compression magnets at proper target positions.

The contributions of this study lay the groundwork for further advancements in endoluminal MCA technology. By offering real-time feedback and guidance to reduce the reliance on the surgeons' experience, the MagsL-HUD endoscopic system

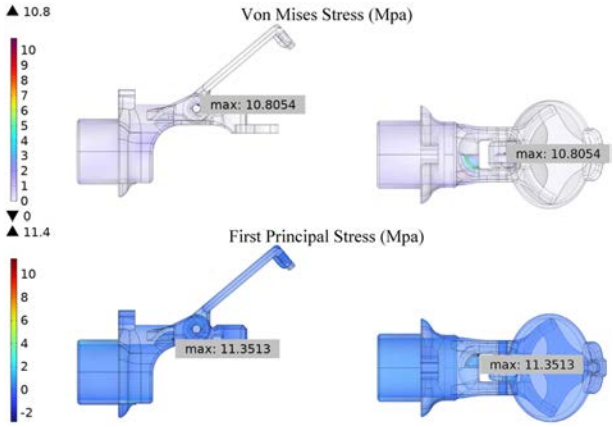

Fig. A1. Illustration of stress evaluation for the 3-D-printed components in Endo-MagCap using FEM simulation, where the maximum stress is marked.

has the potential to make MCA a standardized clinical approach for anastomosis surgeries in unstructured endoluminal environments. With continued research and development, it holds promise for expanding the applicability of MCA surgery to broader clinical scenarios.

Appendix A
Mechanical Analysis of Endo-MagCap

This appendix provides the mechanical analysis of Endo-MagCap and related discussion. As described in Section II-B, the mechanical components of concern is whether the 3-D-printed connector and the up cap meet the stress requirements. First, the torsional spring rate of the spring $k_{\text{rate}} \approx 0.5561$ N · mm/deg. When the Endo-MagCap is in a fire state, the rotation angle $\triangle\theta \approx 70$ deg, resulting in the torque $\tau_{\text{spring}} = k_{\text{rate}}\ \triangle\theta \approx 38.9270$ N· mm. Since the leg length $L_{\text{leg}} = 8$ mm, the max applied force onto the 3-D-printed connector or up cover can be obtained by

$$F_{\text{spring}} = \frac{\tau_{\text{spring}}}{L_{\text{leg}}} \approx 4.8659 \text{ N}.$$

Then, using the FEM method by applying F_{spring} on to the contact faces. Typical 3-D-printed materials that meet ISO 10993 standard, like 3-D-printed PEEK, have tensile strength of about 56 MPa under 50° temperature (which is affected by layer thickness, raster angle, and so on). Here, a conservative value is used as [54]. Since PEEK material is a thermoplastic polymer, both the Von Mises and first principal stresses are examined. Based on the FEM results, which are illustrated in Fig. A1, it can be observed that the maximum Von Mises and first principal stress are 10.8053 and 11.3513 MPa, respectively. It can be obtained that

$$\eta_{sf} = \frac{56}{11.3513} \approx 4.93.$$

Appendix B
Endoscope Calibration Procedure and Results

This appendix provides a detailed procedure employed for the endoscopic calibration. The calibration process, as illustrated in Fig. B1(a), utilizes a checkerboard pattern and the Camera Calibrator toolbox within the MATLAB environment. The procedure is executed as follows.

1) A planar checkerboard with a 10 × 10 grid of squares is generated. Each square was designed with a precise side length of 5 mm.
2) The endoscope system is used to capture a series of images of the checkerboard pattern. To ensure a robust calibration, the endoscope is positioned at various perspectives relative to the checkerboard. Care is taken to maintain the entire checkerboard within the view for each captured image. The captured images are subsequently transferred to a computer via an SDI capture.
3) The captured images are imported into the MATLAB Camera Calibrator toolbox. The toolbox is configured with the known dimensions of the checkerboard squares (5 mm). The software then automatically detects the corners of the checkerboard squares in each image, as depicted in Fig. B1(b).
4) Using the detected checkerboard corners, the calibration function within the toolbox is executed. This function estimates the camera's intrinsic matrix, which includes the focal length and principal point.

The final calibration results are listed in Table B1. Based on practical experience, parameters can contain errors from the endoscope optics, SDI capture, and transmission. Critically, adjustable-focus endoscopes should use the same focal length modes during calibration and application.

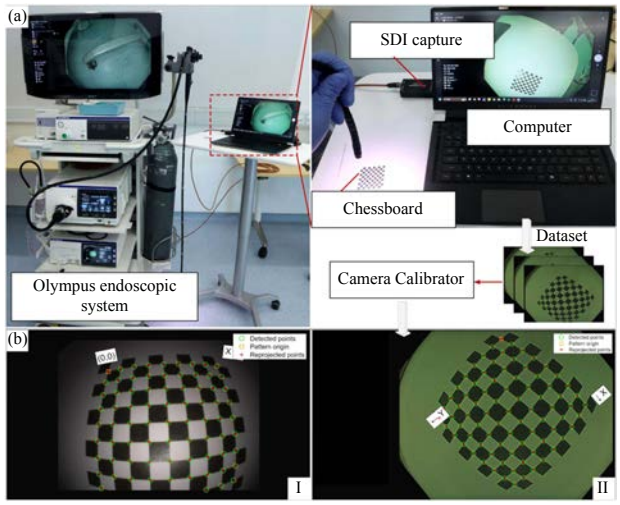

Fig. B1. Illustration of endoscopes' calibration setup and results. (a) Setup for endoscopes' camera calibration. Endoscope image datasets are acquired using SDI capture and calibrated using the Camera Calibrator toolbox in MATLAB. (b) Checkerboard detection results for the endoscopes' camera.

TABLE B1
Endoscopic Camera Intrinsic Matrixes Parameters

	$f_{x,i}$	$f_{y,i}$	$c_{x,i}$	$c_{y,i}$
Gastroscope ($i = 1$)	756.18	752.93	948.11	553.43
Colonoscope ($i = 2$)	770.76	769.27	1236.10	533.44

ACKNOWLEDGMENT

The authors would like to thank the support from AIR@INNOHK Multiscale Medical Robotics Center and Chow Yuk Ho Technology Center for Innovative Medicine. The authors would also like to thank C. Jiang and Z. Jiang for constructive discussions and to R. Lau for support throughout this research.

REFERENCES

[1] K. L. Ong et al., "Global, regional, and national burden of diabetes from 1990 to 2021, with projections of prevalence to 2050: A systematic analysis for the global burden of disease study 2021," *Lancet*, vol. 402, no. 10397, pp. 203–234, 2023.

[2] J. Liu et al., "Projected rapid growth in diabetes disease burden and economic burden in China: A spatio-temporal study from 2020 to 2030," *Lancet Reg. Health West. Pac.*, vol. 33, 2023, Art. no. 100700.

[3] G. Xu et al., "Prevalence of diagnosed type 1 and type 2 diabetes among us adults in 2016 and 2017: Population based study," *BMJ*, vol. 362, 2018, Art. no. k1497.

[4] J. Xie et al., "Global burden of type 2 diabetes in adolescents and young adults, 1990-2019: Systematic analysis of the global burden of disease study," 2019, *BMJ*, vol. 379, 2022, Art. no. e072385.

[5] P. R. Schauer et al., "Effect of laparoscopic Roux-En Y gastric bypass on type 2 diabetes mellitus," *Ann. Surg.*, vol. 238, no. 4, pp. 467–485, 2003.

[6] A. Aminian et al., "Cardiovascular outcomes in patients with type 2 diabetes and obesity: Comparison of gastric bypass, sleeve gastrectomy, and usual care," *Diabetes Care*, vol. 44, no. 11, pp. 2552–2563, 2021.

[7] C. Coelho et al., "Laparoscopic adjustable gastric banding with liraglutide in adults with obesity and type 2 diabetes (GLIDE): A pilot randomised placebo controlled trial," *Int. J. Obes.*, vol. 47, no. 11, pp. 1132–1142, 2023.

[8] E. Machytka et al., "Partial jejunal diversion using an incisionless magnetic anastomosis system: 1-year interim results in patients with obesity and diabetes," *Gastrointest. Endosc.*, vol. 86, no. 5, pp. 904–912, 2017.

[9] G. Zhang, Z. Liang, G. Zhao, and S. Zhang, "Endoscopic application of magnetic compression anastomosis: A review," *J. Gastroenterol. Hepatol.*, vol. 39, no. 7, pp. 1256–1266, 2024.

[10] J. Wall et al., "Magnamosis IV: Magnetic compression anastomosis for minimally invasive colorectal surgery," *Endoscopy*, vol. 45, no. 08, pp. 643–648, 2013.

[11] S. I. Jang, J. Choi, and D. K. Lee, "Magnetic compression anastomosis for treatment of benign biliary stricture," *Dig. Endosc.*, vol. 27, no. 2, pp. 239–249, 2015.

[12] Y. Li et al., "Magnetic compression anastomosis for the treatment of benign biliary strictures: A clinical study from China," *Surg. Endosc.*, vol. 34, pp. 2541–2550, 2020.

[13] C. E. Graves et al., "Magnetic compression anastomosis (magnamosis): First-in-human trial," *J. Amer. Coll. Surg.*, vol. 225, no. 5, pp. 676–681, 2017.

[14] K. D. Gonzales et al., "Magnamosis III: Delivery of a magnetic compression anastomosis device using minimally invasive endoscopic techniques," *J. Pediatr. Surg.*, vol. 47, no. 6, pp. 1291–1295, 2012.

[15] O. Erin, M. Boyvat, M. E. Tiryaki, M. Phelan, and M. Sitti, "Magnetic resonance imaging system–driven medical robotics," *Adv. Intell. Syst.*, vol. 2, no. 2, 2020, Art. no. 1900110.

[16] M.-A. Janvier et al., "Performance evaluation of a medical robotic 3D-ultrasound imaging system," *Med. Image Anal.*, vol. 12, no. 3, pp. 275–290, 2008.

[17] S. E. Salcudean, H. Moradi, D. G. Black, and N. Navab, "Robot-assisted medical imaging: A review," *Proc. IEEE*, vol. 110, no. 7, pp. 951–967, Jul. 2022.

[18] Q. Zhou et al., "Depth-resolved localization microangiography in the NIR-II window," *Adv. Sci.*, vol. 10, no. 1, 2023, Art. no. 2204782.

[19] S. R. Wilson, P. N. Burns, L. M. Wilkinson, D. H. Simpson, and D. Muradali, "Gas at abdominal us: Appearance, relevance, and analysis of artifacts," *Radiol.*, vol. 210, no. 1, pp. 113–123, 1999.

[20] J. Huang, J. K. Triedman, N. V. Vasilyev, Y. Suematsu, R. O. Cleveland, and P. E. Dupont, "Imaging artifacts of medical instruments in ultrasound-guided interventions," *J. Ultrasound Med.*, vol. 26, no. 10, pp. 1303–1322, 2007.

[21] P. Maken and A. Gupta, "2D-to-3D: A review for computational 3D image reconstruction from X-ray images," *Arch. Comput. Methods Eng.*, vol. 30, no. 1, pp. 85–114, 2023.

[22] C. G. Viviers, L. Filatova, M. Termeer, P. H. de With, and F. van der Sommen, "Advancing 6-DoF instrument pose estimation in variable X-ray imaging geometries," *IEEE Trans. Image Process.*, vol. 33, pp. 2462–2476, 2024.

[23] M. S. Linet et al., "Cancer risks associated with external radiation from diagnostic imaging procedures," *CA Cancer J. Clin.*, vol. 62, no. 2, pp. 75–100, 2012.

[24] K. Kwok, N. Hasan, A. Duloy, F. Murad, J. Nieto, and L. W. Day, "American society for gastrointestinal endoscopy radiation and fluoroscopy safety in gi endoscopy," *Gastrointest. Endosc.*, vol. 94, no. 4, pp. 685–697, 2021.

[25] Y. Xu, K. Li, Z. Zhao, and M. Q.-H. Meng, "Adaptive simultaneous magnetic actuation and localization for WCE in a tubular environment," *IEEE Trans. Robot.*, vol. 38, no. 5, pp. 2812–2826, Oct. 2022.

[26] D. Son, S. Yim, and M. Sitti, "A 5-D localization method for a magnetically manipulated untethered robot using a 2-D array of Hall-effect sensors," *IEEE/ASME Trans. Mechatron.*, vol. 21, no. 2, pp. 708–716, 2015.

[27] M. Zhang, L. Yang, C. Zhang, Z. Yang, and L. Zhang, "A 5-D large-workspace magnetic localization and actuation system based on an eye-in-hand magnetic sensor array and mobile coils," *IEEE Trans. Instrum. Meas.*, vol. 72, 2023, Art. no. 7501411.

[28] S. Song, C. Hu, and M. Q.-H. Meng, "Multiple objects positioning and identification method based on magnetic localization system," *IEEE Trans. Magn.*, vol. 52, no. 10, Oct. 2016, Art. no. 9600204.

[29] M. Wang, S. Song, J. Liu, and M. Q.-H. Meng, "Multipoint simultaneous tracking of wireless capsule endoscope using magnetic sensor array," *IEEE Trans. Instrum. Meas.*, vol. 70, 2021, Art. no. 7502510.

[30] K. S. Pečečnik, S. Tomažič, and J. Sodnik, "Design of head-up display interfaces for automated vehicles," *Int. J. Hum. Comput. Stud.*, vol. 177, 2023, Art. no. 103060.

[31] S. Rebensky, M. Carroll, W. Bennett, and X. Hu, "Impact of heads-up displays on small unmanned aircraft system operator situation awareness and performance: A simulated study," *Int. J. Hum.-Comput. Interact.*, vol. 38, no. 5, pp. 419–431, 2022.

[32] H. H. Shishavan, M. M. Behzadi, D. J. Lohan, E. M. Dede, and I. Kim, "Closed-loop brain machine interface system for in-vehicle function controls using head-up display and deep learning algorithm," *IEEE Trans. Intell. Transp. Syst.*, vol. 25, no. 7, pp. 6594–6603, Jul. 2024.

[33] X. Zhang, E.-M. Otoo, Y. Fan, C. Tao, T. Wang, and K. Rhode, "Autostereoscopic 3D augmented reality navigation for laparoscopic surgery: A preliminary assessment," *IEEE. Trans. Biomed. Eng.*, vol. 70, no. 4, pp. 1413–1421, Apr. 2023.

[34] J. I. Liounakos, T. Urakov, and M. Y. Wang, "Head-up display assisted endoscopic lumbar discectomy–A technical note," *Int. J. Med. Robot. Comput. Assist. Surg.*, vol. 16, no. 3, 2020, Art. no. e2089.

[35] M. Birlo, P. E. Edwards, M. Clarkson, and D. Stoyanov, "Utility of optical see-through head mounted displays in augmented reality-assisted surgery: A systematic review," *Med. Image Anal.*, vol. 77, 2022, Art. no. 102361.

[36] J. J. Abbott, E. Diller, and A. J. Petruska, "Magnetic methods in robotics," *Annu. Rev. Control Robot. Auton. Syst.*, vol. 3, no. 1, pp. 57–90, 2020.

[37] S. L. Charreyron, Q. Boehler, B. Kim, C. Weibel, C. Chautems, and B. J. Nelson, "Modeling electromagnetic navigation systems," *IEEE Trans. Robot.*, vol. 37, no. 4, pp. 1009–1021, Aug. 2021.

[38] D. von Arx, C. Fischer, H. Torlakcik, S. Pané, B. J. Nelson, and Q. Boehler, "Simultaneous localization and actuation using electromagnetic navigation systems," *IEEE Trans. Robot.*, vol. 40, pp. 1292–1308, 2023.

[39] S. Su, S. Yuan, M. Xu, H. Gao, X. Yang, and H. Ren, "Amagposenet: Real-time six-DoF magnet pose estimation by dual-domain few-shot learning from prior model," *IEEE Trans. Ind. Inform.*, vol. 19, no. 9, pp. 9722–9732, 2023.

[40] J. L. Blanco-Claraco, "A tutorial on $\mathbf{SE}(3)$ transformation parameterizations and on-manifold optimization," University of Malaga, Málaga, Spain, Tech. Rep. #012010, 2010.

[41] Z. Zhang, "A flexible new technique for camera calibration," *IEEE Trans. Pattern Anal. Mach. Intell.*, vol. 22, no. 11, pp. 1330–1334, Nov. 2000.

[42] A. Fedorov et al., "3D slicer as an image computing platform for the quantitative imaging network," *Magn. Reson. Imag.*, vol. 30, no. 9, pp. 1323–1341, 2012.

[43] G. Zhao et al., "Optimized force range of magnetic compression anastomosis in dog intestinal tissue," *J. Pediatr. Surg.*, vol. 54, no. 10, pp. 2166–2171, 2019.

[44] X. Yu, J. Wang, J. Su, and S. Song, "Inchworm-like biomimetic magnetic-driven robotic shell for capsule endoscope in a tubular environment," *IEEE/ASME Trans. Mechatron.*, vol. 30, no. 3, pp. 2234–2244, Jun. 2025.

[45] M. Gagner, T. Krinke, M. Lapointe-Gagner, and J. Buchwald, "Side-to-side duodeno-ileal magnetic compression anastomosis: Design and feasibility of a novel device in a porcine model," *Surg. Endosc.*, vol. 37, no. 8, pp. 6197–6207, 2023.
[46] T. Kamada et al., "New technique for magnetic compression anastomosis without incision for gastrointestinal obstruction," *J. Amer. Coll. Surg.*, vol. 232, no. 2, pp. 170–177, 2021.
[47] J. Zhang et al., "Magnetic gastrointestinal anastomosis technique for the treatment of duodenal stricture: The first clinical report," *Endoscopy*, vol. 57, no. S 01, pp. E656–E657, 2025.
[48] S. Su, X. Yang, Z. Li, and H. Ren, "A real-time self-sensing approach to sensor array configuration fusing prior knowledge for reconfigurable magnetic tracking systems," *IEEE/ASME Trans. Mechatron.*, vol. 30, no. 3, pp. 2084–2095, Jun. 2025.
[49] M. Brockdorff et al., "Hybrid trajectory planning of two permanent magnets for medical robotic applications," *Int. J. Robot. Res.*, vol. 44, no. 2, pp. 273–290, 2024.
[50] G. Pittiglio, M. Brockdorff, T. da Veiga, J. Davy, J. H. Chandler, and P. Valdastri, "Collaborative magnetic manipulation via two robotically actuated permanent magnets," *IEEE Trans. Robot.*, vol. 39, no. 2, pp. 1407–1418, Apr. 2023.
[51] M. Juřík, J. Kuthan, J. Vlček, and F. Mach, "Positioning uncertainty reduction of magnetically guided actuation on planar surfaces," in *Proc. Int. Conf. Robot. Autom.*, 2019, pp. 1772–1778.
[52] M. Brockdorff et al., "Hybrid trajectory planning of two permanent magnets for medical robotic applications," *Int. J. Robot. Res.*, vol. 44, no. 2, pp. 273–290, 2025.
[53] L. Amoudruz and P. Koumoutsakos, "Independent control and path planning of microswimmers with a uniform magnetic field," *Adv. Intell. Syst.*, vol. 4, no. 3, 2022, Art. no. 2100183.
[54] W. Wu, P. Geng, G. Li, D. Zhao, H. Zhang, and J. Zhao, "Influence of layer thickness and raster angle on the mechanical properties of 3D-printed PEEK and a comparative mechanical study between PEEK and ABS," *Materials*, vol. 8, no. 9, pp. 5834–5846, 2015.

Yichong Sun (Student Member, IEEE) received the B.Eng. degree in mechanical engineering and automation from Chongqing University, Chongqing, China, in 2020, and the M.Eng. degree in mechanical engineering from the Harbin Institute of Technology, Harbin, China, in 2022. He is currently working toward the Ph.D. degree in robotics with the Department of Surgery, The Chinese University of Hong Kong, Hong Kong.

His research interests include medical robotics, robot design and control, and surgical perception.

Yitian Xian (Member, IEEE) received the M.Sc. degree in robotics with Distinction from the University of Bristol, Bristol, U.K., in 2019, and the Ph.D. degree in neurosurgical robot from The Chinese University of Hong Kong, Hong Kong, in 2025.

His research interests include medical robots and systems, as well as their safe, intuitive, and intelligent collaboration with surgeons, particularly in the field of neurosurgery.

Ruoyu Xu received the B.S. degree in mechanical design, manufacturing and automation from the Hefei University of Technology, Hefei, China, in 2015, the M.S. degree in mechanical engineering from the Huazhong University of Technology, Wuhan, China, in 2018, and the Ph.D. degree in computer and information engineering from The Chinese University of Hong Kong, Shenzhen, in 2024.

He is currently a Research Assistant Professor with the Department of Surgery, The Chinese University of Hong Kong, Hong Kong. His current research interests inlude robot design, motion control, and magnetic localization and actuation for medical robotics.

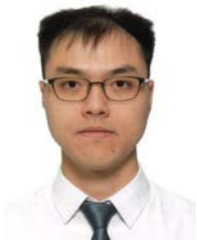

Wai Shing Chan (Graduate Student Member, IEEE) is currently working toward the M.Phil. degree in surgery with the Department of Surgery, The Chinese University of Hong Kong, Hong Kong.

He has three years' experience in medical robotics and took part in the design and modeling of multiple projects. His research interests include medical robotics and magnetic-guided system. His current research focuses on dynamic tissue manipulation with a robot-assisted magnetic countertraction device for endoluminal surgical interventions.

Hon Chi Yip received the MBChB degree (with honors) from the Chinese University of Hong Kong, Hong Kong, in 2008.

He is currently an Assistant Professor with the Department of Surgery, The Chinese University of Hong Kong. He joined the Department of Surgery with the Prince of Wales Hospital after graduation and obtained the Fellowship in General Surgery in 2015. His current research interests include endoscopic diagnosis and treatment of early gastrointestinal cancer, as well as minimally invasive and robotic techniques in surgical treatment of gastric and esophageal neoplasia.

Prof. Yip was the recipient of the RC Li Gold Medal in Surgery.

Philip Wai Yan Chiu received the MBChB degree in medicine and the M.D. degree in surgery from The Chinese University of Hong Kong, Hong Kong, in 1994 and 2009, respectively.

He is currently a Full Professor with the Department of Surgery, the Dean of the Faculty of Medicine, and the Director of the Jockey Club Minimally Invasive Surgical Skills Center and the Multiscale Medical Robotics Center. His research interests include endoscopic surgery, minimally invasive surgery, and robotic surgery.

Zheng Li (Senior Member, IEEE) received the Ph.D. degree in robotics from The Chinese University of Hong Kong, Hong Kong, in 2013.

He is currently a Full Professor with the Department of Surgery, Chow Yuk Ho Technology Centre for Innovative Medicine, Li Ka Shing Institute of Health Science and Multiscale Medical Robotics Center, The Chinese University of Hong Kong. His research interests include design, kinematic modeling, sensing, and control of flexible and soft robots for medical applications.